Showcasing research from Professor Subodh Kumar's laboratory, Department of Chemistry, Guru Nanak Dev University, Amritsar, Punjab, India.

Protonation- and electrostatic-interaction-based fluorescence probes for the selective detection of picric acid (2,4,6-trinitrophenol) – an explosive material

The nitroaromatic explosive materials are putative fluorescence quenchers and generate the non-distinctive spectral signatures. The manuscript highlights that increased proximity between picrate anion and positively charged fluorescent probe due to electrostatic interactions enhances electron or energy transfer processes and thus the quenching efficiency. These features enable selective recognition of picric acid in solid, solution, and vapor phases. This account provides a benchmark for the future design of fluorescent probes for picric acid.

ROYAL SOCIETY OF CHEMISTRY

rsc.li/materials-advances

REVIEW

Check for updates

Protonation- and electrostatic-interaction-based fluorescence probes for the selective detection of picric acid (2,4,6-trinitrophenol) – an explosive material

Sukhvinder Dhiman, [ID] Nancy Singla, [ID] Manzoor Ahmad, [ID] Prabhpreet Singh [ID] and Subodh Kumar [ID] *

Picric acid, due to its low pK_a value, possesses distinct physicochemical features from all other nitroaromatic derivatives, enabling the design of fluorescent probes for its sensitive and selective detection. The electrostatic interactions between the positive charge on the fluorescent probe, which arises due to protonation or the presence of a quaternary nitrogen, and the picrate anion increase the proximity between the fluorescent probe and the analyte, thus increasing the efficiency of the electron or energy transfer processes. This provides a salient feature for the design of fluorescent probes for the selective detection of picric acid over other nitroaromatic compounds. Here, the literature on the use of fluorescent small organic molecules for the selective detection of picric acid based on electrostatic interactions between positively charged/protonated fluorophores and their ability to selectively detect picric acid has been discussed. The fluorescent probes have been classified into three broad categories – neutral fluorophores, which are selectively protonated by picric acid; positively charged probes, which exhibit electrostatic interactions with the picrate anion; and metal complexes with protonatable sites. This comprehensive review will prove a benchmark for the future design of fluorescent probes for picric acid.

1. Introduction

Anti-terrorism and security concerns at places of people movement and other locations have necessitated the development of methods for the trace detection of hazardous explosive materials. The nitroaromatic compounds (NACs) constitute a broad class of widely used explosive materials. In recent years, fluorescence-based detection of NACs has received remarkable attention due to its ease of execution, high sensitivity and the compatibility of technique with the solution, solid and vapor state. These nitroaromatic compounds can be classified into two major categories: (i) phenolic nitroaromatic compounds and (ii) non-phenolic nitroaromatic compounds (Chart 1). Structurally, these nitroaromatic compounds are electron-deficient π-systems, and in general, electron deficiency increases with the increase in the number of nitro groups on the benzene ring.

The phenolic nitroaromatic compound 2,4,6-trinitrophenol (TNP), which is also known as picric acid (PA), is superior to even TNT in energy content and was widely used as an explosive

material during the World Wars.[1,2] PA finds applications in the manufacture of colored glass and the synthesis of dyes.[3,4] It is also a key component in the rocket fuel, matchbox, electric battery and fireworks industries.[5] Due to these industries, PA is released into the environment *via* anthropogenic activities, resulting in its presence in wastewater, aquatic systems[6] and soil[7] and as a contaminant in the air. Its high solubility in basic solutions and water (12.7 g l^{-1})[8] and estimated soil absorption coefficient of 180 can lead to its easy transfer into the environment *via* groundwater, soil *etc.*[9] PA causes skin sensitization, immuno-toxicity and methemoglobinemia, headaches, liver damage, and anemia in humans and can also have a negative effect on the respiratory organs due to the effects of bio-amplification and bioaccumulation. It is a dermal sensitizer and strong eye irritant for animals such as rats.[10,11] Additionally, PA can be metabolised to picramic acid, which has a higher mutagenic activity than PA itself.[12] PA can also be degraded by the *Rhodococcus* sp. strain in PA-contaminated soil.[13]

In the literature, fluorescence-based molecular probes for the detection of NACs have been reviewed, but in not even a single case has the focus been on the selective recognition of picric acid.[14,15]

Conventional analytical methods, including chromatographic methods such as gas chromatography[16] and liquid

Department of Chemistry, Center of Advanced Studies, Guru Nanak Dev University, Amritsar – 143 005, India. E-mail: subodh_gndu@yahoo.co.in, subodh.chem@gndu.ac.in
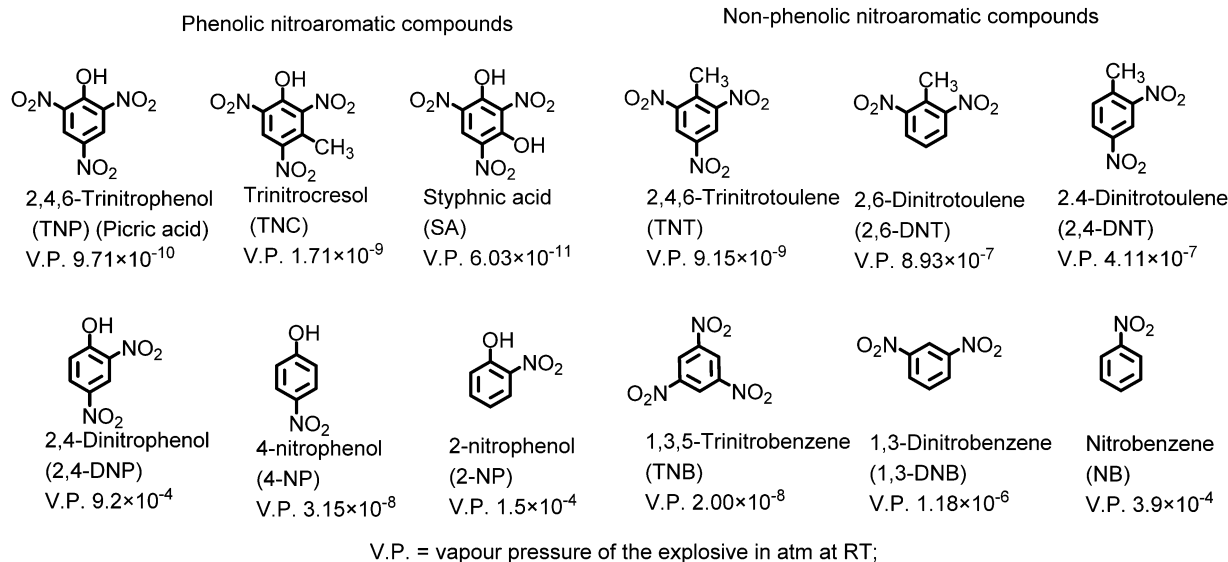
Phenolic nitroaromatic compounds

Non-phenolic nitroaromatic compounds

2,4,6-Trinitrophenol
(TNP) (Picric acid)
V.P. 9.71×10^{-10}

Trinitrocresol
(TNC)
V.P. 1.71×10^{-9}

Styphnic acid
(SA)
V.P. 6.03×10^{-11}

2,4,6-Trinitrotoulene
(TNT)
V.P. 9.15×10^{-9}

2,6-Dinitrotoulene
(2,6-DNT)
V.P. 8.93×10^{-7}

2,4-Dinitrotoulene
(2,4-DNT)
V.P. 4.11×10^{-7}

2,4-Dinitrophenol
(2,4-DNP)
V.P. 9.2×10^{-4}

4-nitrophenol
(4-NP)
V.P. 3.15×10^{-8}

2-nitrophenol
(2-NP)
V.P. 1.5×10^{-4}

1,3,5-Trinitrobenzene
(TNB)
V.P. 2.00×10^{-8}

1,3-Dinitrobenzene
(1,3-DNB)
V.P. 1.18×10^{-6}

Nitrobenzene
(NB)
V.P. 3.9×10^{-4}

V.P. = vapour pressure of the explosive in atm at RT;

Chart 1 Structures of phenolic and non-phenolic nitroaromatic compounds.

chromatography,[17] mass spectrometry,[18] electrochemical techniques[19] and Raman spectroscopy[20] have been applied for the recognition of picric acid, but have found find limited use due to their low sensitivity, interference from other compounds sample pre-treatment requirements, use of expensive and sophisticated equipment, lack of portability, and difficult on-site operation. Numerous fluorescence-based platforms involving small organic molecules, supramolecules,[21] metal complexes,[22] metal organic frameworks (MOFs),[23] and quantum dots/nanoclusters,[24,25] coordination polymers,[26] among others, have been synthesized for the real-time detection of picric acid.

In order to improve the sensitivity of fluorescent sensors towards PA, the primary focus must be either increasing the quenching efficiency by increasing the binding affinity for picric acid, or increasing the energy/electron transfer rate between the fluorophore and PA through appropriate design. The ability of picric acid (pK_a 0.42)[27] to protonate basic sites such as amines or heterocyclic nitrogens present in the fluorophore can induce electrostatic interactions between the protonated fluorophore and the picrate anion. Further, due to its low pK_a value, PA remains in dissociated form in water or buffer solutions and electrostatic interactions can form between positively charged fluorescent probes and the picrate anion. Such electrostatic interactions lead to proximity between the electron-rich fluorophore and the picrate anion and positively affect the electron/energy transfer process and sensitivity of the probe toward picric acid. The general mechanistic approach involved in the selective detection of picric acid by such fluorophores is presented in Scheme 1. Other nitrophenol derivatives have poor electron/energy transfer processes in comparison to picric acid, which is due to the difficulty in the protonation of the basic site(s) in the fluorophore in the case of 2,4-DNP (pK_a 4.04) and 4-NP (pK_a 7.07) and the absence of electrostatic interactions in the case of neutral NACs; thus, they may not interfere in the detection of picric acid.

Generally, fluorophores without any protonation sites undergo fluorescence quenching with TNT and PA with equal ease[28–30] and display strong TNT-interference in the detection of picric acid. Furthermore, there are number of references in which the quenching of a fluorophore by PA has been evaluated, but the effect of other NACs has not been studied.[31,32] Such literature has been omitted in the present discussion.

The discussion of the fluorescent probes (listed in Table 1–4) for picric acid has been classified into following sections:

2. Neutral fluorescent probes for the detection of picric acid

2.1 Protonation of amine-based fluorescent probes for picric acid

2.2 Protonation of pyridine-based fluorescent probes for picric acid

2.3 Protonation of imidazole-based fluorescent probes for picric acid

2.4 Protonation of imine-based fluorescent probes for picric acid

2.5 Protonation of amide-based fluorescent probes for picric acid

3. Positively charged probes for the detection of picric acid

3.1 Monopodal cationic fluorescent probes for picric acid

3.2 Dipodal dicationic fluorescent probes for picric acid

4.3 Tripodal tricationic fluorescent probes for picric acid

4. Metal complexes for the detection of picric acid

44. Miscellaneous

2. Neutral fluorescent probes for the detection of picric acid

In this section, the fluorescent probes **1–28**[33–54] (Charts 2–4) undergo protonation by picric acid at the amine nitrogen to form quaternary anilinium picrate salts, and electron or energy transfer from the photo-excited probe to PA results in the formation of a non-emitting complex. However, the strong
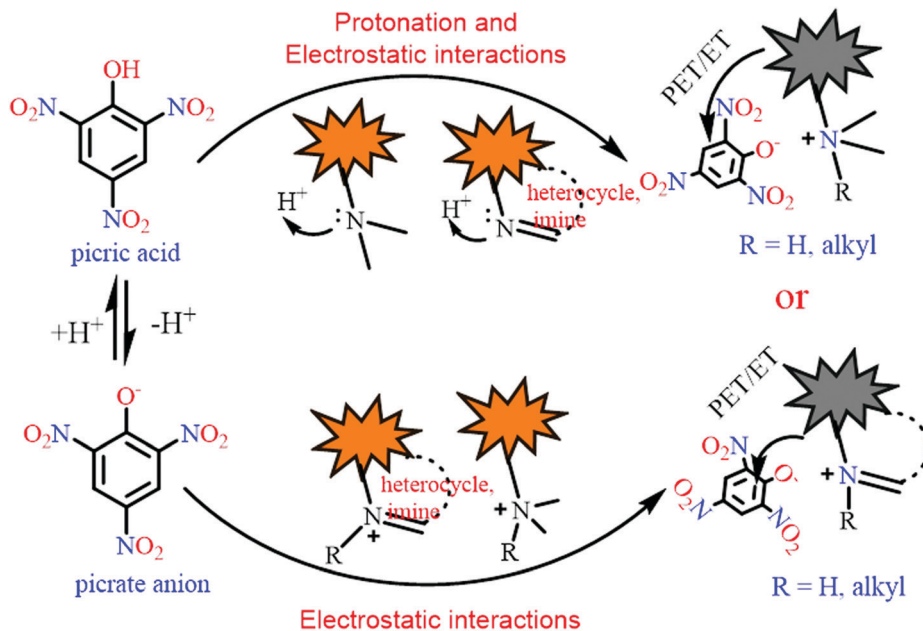
Scheme 1 A schematic presentation of the mechanisms involved in the selective fluorescence quenching of different probes by picric acid.

inhibition of PET in BODIPY-based probe **25**[52] and the aggregation of curcumin-based probes **27** and **28**[54] upon protonation with picric acid result in fluorescence enhancement. A comparison of the solvents, LODs, K_{SV} values, emission maxima and applications of probes **1–28** has been presented in Table 1.

2.1 Protonation of amine-based fluorescent probes for picric acid

Hexa-*peri*-hexabenzocoronene (HBC) probes **1** and **2**[33] (Chart 2) formed spherical nano-aggregates with respective diameters of 200 and 150 nm and exhibited 67% and 85% enhancements in fluorescence intensity between 460–600 nm in water–THF (4:6) owing to the restriction in rotation. Further increasing the amount of water caused lowered emission intensity due to π–π interactions between the coronene cores. Probe **1** exhibited 98% fluorescence quenching in water–THF (4:6) at pH 7.0, turning from a yellow fluorescent solution to a non-fluorescent one with 5 equivalents of PA. The formation of an electrostatic complex by proton transfer from PA to the basic amino group and electron transfer from photo-excited **1** to PA were responsible for the formation of the non-emitting complex. As the pH of the solution was lowered, the quenching efficiency of **1** by PA gradually decreased owing to the weaker interaction of PA with protonated NH$_2$ and reduced electron transfer from the excited-state HBC core to PA. Probe **2** with no protonation site showed lower quenching efficiency by PA, and its ability to interact with PA remained unaffected by lowering of the pH of the solution. Probe **2** underwent fluorescence quenching by PA through an intermolecular charge transfer mechanism. Test paper strips coated with solutions of **1** and **2** detected PA by contact modes. A solution of **1** could detect PA vapor through fluorescence quenching.

Naphthyridine-based fluorescent probes **3** and **4**[34] (Chart 2) were used for the detection of PA in both pure methanol and aqueous methanol solutions. Probes **3** and **4** showed complete fluorescence quenching with 4.5 and 4.0 equivalents of PA, respectively, due to the protonation of the amine and H-bonding between the nitrogen atom of the naphthyridine ring and PA. Similar fluorescence quenching of **3** and **4** was observed for 22 equivalents of 4-NP and significantly higher amounts of other NACs. Probes **3** and **4** formed ground-state complexes with PA and followed static quenching processes. TLC plates coated with probes **3** and **4** with PA exhibited a change in fluorescence colour from blue to non-fluorescent (Fig. 1).

Anthracenecarboxamide-based probe **5a**[35] (Chart 2) exhibited fluorescence quenching with 5 equivalents of nitrophenols; the fluorescence quenching followed the order PA (>96%) > 2,4-DNP (35%) > 3,4-DNP (17%) > 4-DNP (10%) in ethanol. A Job's plot analysis showed 1:1 complexation between probe **5a** and PA with an association constant of 4.14×10^5 M^{-1}. Probes **5b** and **5c** also showed formation of a 1:1 complex with lower binding constant values of 3.34×10^4 M^{-1} and 5.95×10^3 M^{-1}, respectively. The ^{1}H NMR downfield shift of the amide proton from δ 8.91 to 9.55 ppm and of the imidazole C2–H from δ 7.68 to 9.05 ppm for probe **5a** upon the addition of PA revealed its multiple hydrogen bonding with PA. The fluorescence quenching of probes **5a–5c** by PA could be assigned to multiple factors, including FRET, H-bonding and π–π interactions.

Calix[4]arene-based probe **6**[36] (Chart 2) with aminonaphthalimide moieties conjugated at the 1 and 3 aryl rings displayed 97% fluorescence quenching at 520 nm (λ_{ex} = 410 nm) by PA and resulted in a fluorescence colour change from green to non-florescent and a decrease in the quantum yield from 0.33 to 0.02. 4-Nitrophenol and neutral NACs did not cause any considerable fluorescence quenching of **6**. The protonation of the amine by PA inhibited ICT and resulted in non-fluorescent complex formation. AFM studies revealed that

Table 1 A comparison of solvent, LOD, K_{SV}, emission maxima, and application data for amine-based probes **1–28**

S. no.	Probe	Solvent	LOD (µM)	K_{SV} (M^{-1})	λ_{ex} (nm)	λ_{em} (nm)	Applications	Ref.
Protonation of amine-based fluorescent probes for picric acid								
1	**1**	THF–H$_2$O (6:4)	0.004	3.2×10^6	368	485	Paper strips	33
					398	510		
2	**2**	THF–H$_2$O (6:4)	0.009	2.0×10^6	370	—	Paper strips	33
3	**3**	CH$_3$OH	4.89	7.203×10^4	340	385	TLC plate	34
		H$_2$O–CH$_3$OH (8:2)						
4	**4**	CH$_3$OH	4.16	3.903×10^4	345	397	TLC plate	34
		H$_2$O–CH$_3$OH (8:2)						
5	**5a**	EtOH	1	4.14×10^5	362	417	—	35
6	**5b**	EtOH	—	3.34×10^4	362	417	—	35
7	**5c**	EtOH	—	5.95×10^3	362	417	—	35
8	**6**	THF	0.3	4.51×10^5	410	520	Paper strips	36
9	**7**	THF	0.08	1.0×10^5	354	435	Test strips	37
		THF–H$_2$O (1:1)			—	460	TLC plate	
		THF–H$_2$O (1:9)			371	438		
10	**8**	H$_2$O:THF (1:1)	0.04	1.11×10^5	306	393	—	38
11	**9**	H$_2$O:THF (7:3)	0.035	1.95×10^5	322	458	Paper strips	38
12	**10a**	CH$_3$CN	—	1.2×10^5	290	405 to 480	—	39,40
13	**10b**	CH$_3$CN	9.82	2.8×10^5	302	415	—	42
14	**10c**	CH$_3$CN	6.55	3.31×10^5	295	425	—	41
14	**11**	H$_2$O	0.0042	4.82×10^5	460	550	Paper strips	43
							Real sample	
15	**12**	H$_2$O	0.0116	5.232×10^5	550	650	Paper strips	43
							Real sample	
16	**13**	THF	16	0.4×10^4	398	512	Paper strips	44
		THF–H$_2$O (4:6)	2	2.6×10^4		550		
17	**14**	EtOH–H$_2$O (5%)	1.3	—	387	540	—	45
18	**15**	THF	5.7	—	—	454	Paper strips	46
							TLC plate	
19	**16**	THF	—	—	—	454	—	46
20	**17**	EtOH	0.079	6.1×10^3	354	410	—	47
21	**18**	THF–HEPES (4:1)	0.0578	1.05×10^5	366	408	Paper strips	48
							Real sample	
22	**19**	THF	26	—	384 to 400	467 to 576	—	49
		THF–H$_2$O (3:7)	38					
23	**20**	THF	—	—	390	471	—	49
		THF–H$_2$O (3:7)			400 → 490	490		
24	**21**	THF	—	—	392	490 → 540	—	49
		THF–H$_2$O (3:7)			400 → 490			
25	**22**	THF	—	—	402	490 → 540	—	49
		THF–H$_2$O (3:7)			400 → 490			
26	**23**	CH$_3$CN	7.2.	1.4×10^4	260	350	—	50
						520		
27	**24**	CH$_3$CN–H$_2$O (8:2)	0.44	—	365	540	—	51
28	**25**	EtOH	0.0028	1.91×10^4	499	513	—	52
29	**26**	DMSO:H$_2$O (1:4)	0.0032	4.37×10^4	367	496 to 454	Real water sample	53
							Paper strips	
30	**27**	Aqueous media	0.0135	—	430	540	Real sample	54
31	**28**	Aqueous media	0.0135	—	430	535	Real sample	54

the donut-like structures of **6** were transformed into extended ribbon-like structures (Fig. 2A) with a length of several microns, a width of 100–160 nm, and a height of 35–45 nm upon treatment with PA. A solution of **6** and cellulose filter paper strips coated with probe **6** (Fig. 2B) could detect 0.3 µM and 0.1 µM PA, respectively, as the lowest limits.

Hydrazono-sulfonamide adduct **7**[37] (Chart 2), which is weakly emissive in THF, became strongly emissive with a maximum between 434–460 nm upon the addition of 50–100% water, owing to the inhibition of C=N isomerization. Solutions of **7** in THF, THF–water (1:1) and THF–water (1:9) exhibited complete fluorescence quenching by 50, 30 and 30 equivalents of PA, respectively. However, the Stern–Volmer constant (1.0 × 10^5 M^{-1}) was highest in the THF–water (1:1) mixture. In the

THF–water (1:1) mixture, the aggregates of **7** formed a greater number of voids to interact with PA, and this loose packing was responsible for the higher sensing performance compared to that observed in other solvents. The quenching efficiency of nitrophenols followed the order PA > 4-NP > 2,4-DNP. The protonation of the dimethylarylamine nitrogen associated with electron transfer from the excited state of fluorophore **7** to PA was responsible for the fluorescence quenching.

Triphenylene derivatives **8** and **9**[38] revealed a 1.5- to 1.6-fold fluorescence enhancement in an H$_2$O–THF (7:3) mixture owing to the formation of aggregates (Fig. 3A and B) and the restriction of TICT. The fluorescent aggregates of **8**[38] (Chart 2) with 20 equivalents PA in an H$_2$O–THF (1:1) mixture displayed 98% fluorescence quenching following the energy transfer

Table 2 A comparison of solvent, LOD, K_{SV}, emission maxima, and application data for pyridine-based probes **29–60**

Protonation of pyridine-based fluorescent probes for picric acid

S. no.	Probe	Solvent	LOD (μM)	K_{SV} (M^{-1})	λ_{ex} (nm)	λ_{em} (nm)	Applications	Ref.
1	**29a**	H$_2$O–DMSO (1:1)	0.720	3.40×10^3	310	481	Paper strips	55
2	**29b**	H$_2$O–DMSO (1:1)	0.650	4.36×10^3	310	481	Paper strips	55
3	**29c**	H$_2$O–DMSO (1:1)	0.600	6.52×10^3	310	492	Paper strips	55
4	**30**	H$_2$O–THF (9:1)	0.250	8.44×10^3	300	475, 555	Paper strips	55
5	**31**	H$_2$O–THF (9:1)	0.290	3.61×10^3	300	475, 555	Paper strips	55
6	**32**	H$_2$O–EtOH (6:4)	0.026	—	273	339 to 460	Paper strips	56
7	**33**	H$_2$O–EtOH (3:7)	—	—	273	339 to 460	—	56
8	**34**	H$_2$O–EtOH (6:4)	—	—	290	345	—	56
9	**35**	CHCl$_3$	0.131–0.294	2.54×10^4	334	417	Paper strips	57
10	**36**	CHCl$_3$	0.131–0.294	2.63×10^4	339	435	Paper strips	57
11	**37**	CHCl$_3$	0.131–0.294	2.69×10^4	341	437	Paper strips	57
12	**38**	CHCl$_3$	0.131–0.294	8.08×10^4	390	498	Paper strips	57
13	**39**	Hydrosol	0.43	7.8×10^4	315	359	—	58
14	**40**	MeOH	0.056	—	—	405 to 522	—	59
15	**41**	H$_2$O–DMSO (1:1)	0.063	—	—	530	Smartphone device	60
16	**42**	DMSO–H$_2$O (1:99)	0.0315	2.3×10^6	380	527	Water sample, test strips	61
17	**43**	DMSO–H$_2$O (1:1)	0.013	7.69×10^4	375	522	Real sample	62
18	**44**	THF	1.747	4.106×10^5	350 to 424	440 to 550	—	63
19	**45**	CH$_3$CN–H$_2$O (4:1)	0.5	4.4×10^5	330	410	Water sample	64
20	**46**	THF	2.184	4.3×10^4	360 to 500	500	Paper strips TLC plates	65
21	**47**	MeOH : H$_2$O (8:2)	100.4	—	400	500	—	66
22	**48**	DMF	0.108	3.86×10^5	419	483	—	67
23	**49**	DMF	0.138	3.21×10^5	369	420	—	68
24	**50**	DMF	0.102	4.65×10^5	353	448	—	68
25	**51**	DMF	0.196	1.57×10^5	335	416, 559	—	68
26	**52**	EtOH	0.075	4.15×10^5	500	545	Paper strips	69
		H$_2$O	0.570	3.94×10^4	400	542		
27	**53**	EtOH	0.110	2.5×10^5	517	558	Paper strips	69
		H$_2$O	0.93	2.1×10^4	400	555		
28	**54**	H$_2$O	2.62	5.78×10^4	—	420	Paper strips	70
29	**55**	H$_2$O	6.98	3.26×10^4		450	Paper strips	70
30	**56**	MeOH	0.0056	6.87×10^4	490	537, 576, 627	—	71
31	**57**	CH$_3$CN	0.644	3.45×10^5	365	493	Test strips	72
		H$_2$O	0.586	2.18×10^5	365	460		
32	**58**	CH$_3$CN	—	—	365	438	—	72
33	**59a**	EtOH	—	67.6×10^3	370	474	—	73
34	**59b**	EtOH	—	60.3×10^3	370	474	—	73
35	**59c**	EtOH	—	74.2×10^3	370	474	—	73
36	**59d**	EtOH	—	62.2×10^3	370	474	—	73
37	**60**	CH$_3$CN–H$_2$O (1:9)	0.0373	6.4×10^7	540	581	Paper strips, water samples	74

process at 393 nm, as observed from the overlap of the fluorescence spectrum of **8** with the absorbance spectrum of PA. The aggregates of **9** with 26 equivalents of PA in an H$_2$O–THF (7:3) mixture exhibited fluorescence quenching at 458 nm due to the protonation of the basic NH$_2$ groups and electrostatic interactions between the protonated aggregates of **9** and the picrate anion. Probe **9** displayed higher selectivity towards PA than derivative **8**. Paper strips coated with **9** (Fig. 3C) could detect 10^{-11} M PA. Other NACs such as TNT, 2,4-DNT, 1,4-DNB, NB, 4-NT, BQ, NM and DMNB caused fluorescence quenching, but at significantly higher concentrations.

The C3-symmetric 1,3,5-tris(4′-aminophenyl)benzene **10a**[39,40] (Chart 2) exhibited a red shift in its emission maximum from 405 nm to 480 nm due to PA. A solution of **10a** with 32 equivalents of PA and 450–640 equivalents of TNT, DNT and 1,4-DNB exhibited > 80% quenching of fluorescence intensity, pointing to the selective fluorescence quenching by PA (Fig. 4A). The X-ray crystal structures of **10a** with PA (Fig. 4B) and TNT revealed the formation of 1:1 stoichiometric complexes through

strong intermolecular π–π interactions between **10a** and the NACs. The layers of the probe could intercalate three molecules of 1,3-DNB. The crystal lattices are further stabilized through inter-stack hydrogen bonds (N–H···N and N–H···O) between the amino groups of the probe and nitro groups of the NACs (Fig. 4B). Thin films prepared from **10a** could detect TNT and DNT vapor, but not PA vapor.

Probe **10c**,[41] which exhibited reduced H-bond donor characteristics in comparison to probe **10a**, but increased basicity of the amine nitrogen, revealed 90% fluorescence quenching with only 10 equivalents of PA in comparison to the 32 equivalents of PA required by probe **10a**. Furthermore, **10c** formed a 1:3 (**10c** ∩ (PA)$_3$) stoichiometric complex through proton transfer from three molecules of PA to the three amine nitrogens of **10c**, as was clearly evident from the X-ray crystal structure (Fig. 4C). However, **10a** formed only a 1:1 stoichiometric complex through H-bonding (Fig. 4B). The association constants of **10c** with NACs followed the order PA ≫ 1,4-DNB > TNT ≈ 2,4-DNT ≈ 1,3-DNB, with PA being almost 25 times more effective

Table 3 A comparison of solvent, LOD, K_{SV}, emission maxima, and application data for imidazole, amide, and imide probes **61–84**

S. no.	Probe	Solvent	LOD (µM)	K_{SV} (M^{-1})	λ_{ex} (nm)	λ_{em} (nm)	Applications	Ref.
Protonation of (benz)imidazole-based fluorescent probes for picric acid								
1	**61**	DMSO–H$_2$O (7:3)	0.17	3.75×10^4	270	392	Water samples	75
2	**62**	EtOH–H$_2$O (7:3)	0.49	2.4×10^4	280	345	Water samples	75
3	**63**	DMSO–H$_2$O (1:9)	3.223	1.168×10^4	312	413	Paper strips	76
4	**64**	DMSO–H$_2$O (1:9)	2.987	2.65×10^4	309	409	Paper strips	76
5	**65**	DMSO–H$_2$O (1:9)	2.996	2.05×10^4	309	401	Paper strips	76
6	**66a**	EtOH	2.8	8.62×10^4	340	386	—	77
7	**66b**	EtOH	2.3	1.45×10^5	340	486	—	77
8	**66c**	EtOH	4.6	8.53×10^4	340	456	—	77
9	**67**	H$_2$O–THF (9:1)	0.0025	2.54×10^5	335	422	Paper strips, water samples	78
10	**68**	THF	0.218	1.115×10^5	300	376	TLC plate Paper strip	79
11	**69**	CHCl$_3$	21.6	5.1×10^4	307	367 to 381	—	80
12	**70b**	CHCl$_3$ Acetone–H$_2$O (1:1)	19.0	9.9×10^6	307	367 to 383	Paper strips	80
13	**71**	Toluene CH$_3$CN	2.515 1.065	6.58×10^4 1.85×10^6	345	378, 397	—	81
14	**72**	H$_2$O–DMF (9:1)	3.55	1.3×10^4	400	574	Mechanochromic behaviour	82
Protonation of imine-based fluorescent probes for picric acid								
15	**73**	CH$_3$CN	0.01	6.814×10^6	368 to 344	425 to 462	Paper strips	83
16	**74**	CH$_3$CN–H$_2$O (2:8)	—	—	390	467	Paper strips	84
17	**75**	THF–H$_2$O (1:9)	0.010	2.03×10^4	375	469	Test strips	85
18	**76**	THF–H$_2$O (1:9)	0.0726	70×10^{-6}	430	585, 620	TLC plate, test strip	86
Protonation of amide-based fluorescent probes for picric acid								
19	**77**	H$_2$O–THF (9:1)	0.47	7.0×10^4	371	558	Filter paper	87
20	**78**	DMSO	0.011	7.40×10^4	370	435	Paper strips	88
21	**79**	PBS buffer	0.0000256	2.20×10^7	338	484	Paper strips, TLC plate	89
22	**80**	THF–H$_2$O (1:9)	3.93	9.6×10^4	350	590	TLC plate	90
23	**81**	THF	2.98	6.02×10^3	455	529	—	91
24	**82**	EtOH	0.820	—	314	420 to 460, 586	Paper strips	92
25	**83a**	MeOH–H$_2$O (1:4)	0.00002	7.05×10^7	480	539 to 581	Water sample	93
26	**83b**	MeOH–H$_2$O (1:4)	—	—	—	—	—	93
27	**84**	MeOH	0.035	—	314	430 to 578	TLC strip-solid PA	94

as a quencher in comparison to the other NACs. Additionally, instead of the PET mechanism operative in the case of probe **10a**, here, proton transfer is the actual quenching mechanism. The quenching efficiency of **10b**[42] was intermediate between those of probes **10a** and **10c**, and their quenching efficiency followed the same order as the basicity of the amine nitrogens. The emission spectrum of **10b** showed 85% quenching of the emission maximum with 20 equivalents of PA with a detection limit of 9.82 µM.

The curcumin-based fluorophores **11** and **12**[43] (Chart 3) with PA exhibited 92 and 93% quenching of the intense emission at 550 nm for **11** and 650 nm for **12**, respectively, with a visible colour change from yellow to red for **11** and pink to bluish green for **12** in the aqueous solution. No change in the FI was observed with the addition of other NACs. The protonation of **11**/**12** by PA and electron transfer from the fluorophore to PA are responsible for fluorescence quenching *via* the static process. The probes were also used to detect PA in water samples.

Probe **13**[44] showed a red shift in its emission maximum from 485 nm to 543 nm when moving from the non-polar solvent toluene to the highly polar solvent methanol, indicating that due to increased ICT, the molecular geometry in the first excited state is more polarized than that in the ground state. A THF–H$_2$O (4:6) solution of **13** displayed the highest emission intensity among the binary solutions owing to the formation of aggregates with restriction in the π–π stacking interactions and intramolecular rotations. The high emission of **13** in THF–H$_2$O

(4:6) decreased by 97.32% upon the addition of 30 equivalents of PA, whereas in pure THF, 95.43% fluorescence quenching was observed with 40 equivalents of PA. The emission quenching mechanism is explained by the electron transfer and/or energy transfer processes. Among PA, 2,4-DNP, 4-NP, TNT, 1,4-DNB and NB, PA had the greatest quenching efficiency (Fig. 5). Paper strips coated with **13** showed a dark spot for 10^{-3} M PA.

α-Cyanostilbene derivative **14**[45] (Chart 3) with 4 equivalents of PA in an ethanol–water (95:5) mixture revealed 60% fluorescence quenching (at 540 nm), but the quenching did not exceed 20% with other NACs. Remarkable acidochromic behaviour was observed with TFA, hydrochloric acid, TEA and/or their vapors due to the basicity of the nitrogen atom. Using mechanical grinding, solvent writing and vapor erasing, a reversible fluorescence switching cycle was observed.

Thiophene-based probes **15** and **16**[46] (Chart 3) were used for the detection of PA and intracellular pH. **15** was more selective for PA as compared to **16**. Probe **15** showed a 30% reduction in emission intensity in THF with 0.1 equivalents of PA and could detect concentrations as low as 5.7 µM PA. Paper strips and TLC plates coated with probe **15** solution detected PA in visible light (colourless to yellow) and under 365 nm (blue fluorescent to non-fluorescent). The compound was also used for the fluorescence-based determination of pH in live cells.

Fluorophore **17**[47] (Chart 3) displayed quenching of its fluorescence intensity with no shift in the emission maximum

Table 4 A comparison of solvent, LOD, K_{SV}, emission maxima, and application data for positively charged probes **85–128**

S. no.	Probe	Solvent	LOD (μM)	K_{SV} (M^{-1})	λ_{ex} (nm)	λ_{em} (nm)	Applications	Ref.
Monopodal positively charged probes for picric acid								
1	**85**	MeOH–H$_2$O (9:1)	4.7	2.38×10^4	430 to 350	580	—	95
2	**86**	MeOH–H$_2$O (9:1))	3.6	1.08×10^4	430 to 350	593	—	95
3	**87**	MeOH–H$_2$O (9:1)	—	—	430	599	—	95
4	**88**	H$_2$O	1.98	—	365	390 to 455	Water sample	96
5	**89**	H$_2$O–THF (1:1)	0.0082	1.67×10^9	550 / 610	620 / 730	Paper strips	97
6	**90**	H$_2$O–THF (1:1)	0.0088	—	460	∼710	Paper strips	97
7	**91**	H$_2$O	0.107	2.2×10^4	325 to 340	480	TLC plate	98
8	**92**	H$_2$O	0.087	5×10^4	325 to 340	410	TLC plate	98
9	**93**	H$_2$O	1.878	—	292	402	—	99
10	**94**	PBS–DMSO (0.5%)	—	5.52×10^3	336	378	—	100
11	**95**	PBS–DMSO (0.5%)	—	6.55×10^4	336	383	—	100
12	**96**	PBS–DMSO (0.5%)	0.00029	8.34×10^6	336	494	Paper strips, water sample	100
13	**97**	CH$_3$CN	0.070	—	620	684 to 644	Paper strips	101
Dipodal positively charged probes for picric acid								
14	**98**	SDS–H$_2$O	1	—	345	480	—	102
15	**99**	Aqueous media, 95%	0.00056	0.1×10^8	325	406	Paper strips	103
16	**100**	H$_2$O	—	1.75×10^4	365	513	—	104
17	**101**	H$_2$O	—	6.04×10^4	365	485	—	104
18	**102**	NMP	1.0	16.8×10^6	337	∼470	—	105
19	**103**	DMF and H$_2$O	1.0	—	370	545, 580	—	106
20	**104**	DMF	1.0	—	370	543	—	106
21	**105**	DMF	1.0	—	370	543	—	106
Tripodal positively charged probes for picric acid								
22	**106**	DMSO	2.039	3.8×10^4	371	399, 422, 446	Water samples	107
23	**107**	DMSO	1.545	3.3×10^4	371	399, 422, 446	Water samples	107
24	**108**	HEPES–DMSO (2%)	—	2.67×10^5	290	402	—	108
25	**109**	HEPES–DMSO (2%)	0.001	3.57×10^5	290	470	Paper strips	108
26	**110**	HEPES–DMSO (2%)	—	—	290	450 to 485	—	108
27	**111**	H$_2$O–DMSO (2%)	0.000005	1.20×10^{11} / 1.10×10^8 / 4.78×10^5	290	402	Paper strips	109
28	**112**	HEPES–DMSO (2%)	0.00001	1.57×10^9	335	520	Paper strips	110
29	**113**	H$_2$O–DMSO (2%)	0.025	6.25×10^5	290	454	Paper strips	111
30	**114**	H$_2$O–DMSO (2%)	0.0000001	2.56×10^{11}	290	448	Paper strips	111
31	**115**	H$_2$O–DMSO (2%)	0.0000001	5.04×10^{11}	290	412	Paper strips	111
32	**116**	H$_2$O–DMSO (2%)	0.0000001	6.73×10^8	335	480	Paper strips	112
33	**117**	H$_2$O	15.2	3.43×10^3	340	∼480	Paper strips	113
34	**118**	HEPES buffer	0.0001 (UV) / 0.003 (FL)	—	490	615	Soil sample	114
35	**119**	HEPES buffer	0.020 (UV) / 0.002 (FL)	—	490	615	Turn-ON Paper strips	115
Metal-complex-based probes for picric acid								
36	**120**	DMSO–H$_2$O (5:95)	0.0121	1.165×10^6	383	485	Paper strips	116
37	**121**	H$_2$O	0.99	5.29×10^4	400	470	Thin film	117
38	**122**	H$_2$O–THF (4:6)	0.03	1.92×10^5	380	460	Paper strips	118
39	**123**	THF–H$_2$O (9:1)	0.170	9×10^4	380	458	—	119
40	**124**	DMSO	3.056	1.6×10^5	630	684, 752	Thin film	120
41	**125**	DMSO	4.803	2.02×10^5	630	696, 761	Thin film	120
Miscellaneous								
42	**126**	Toluene	0.131	2.1×10^6	500	600	Paper strips	121
43	**127**	CH$_3$CN–H$_2$O (9:1)	$0.707 \pm (0.06)$	9.2×10^6	504 to 516	518 to 535	Thin film	122
44	**128**	H$_2$O	0.0172	1.65×10^6	279	348	—	123

with PA in ethanol. The quenching was due to the H-bonding interactions of the NH$_2$ group of **17** with the phenolic –OH group of PA, as the singlet at δ 5.33 ppm for the free NH$_2$ group shifted downfield to δ 6.48 ppm after interaction with PA in the ^{1}H NMR experiment. Probe **17** formed a 1:1 stoichiometric complex with PA with a Stern–Volmer constant of 6.1×10^3 M^{-1}.

Inner filter effect and protonation assisted PET-based detection of PA using conjugated polymer **18** (Chart 4) was developed by Iyer *et al.*[48] Upon excitation of a THF solution of **18** at 366 nm, emission was observed at 408 nm. The fluorescence of

18 in THF–HEPES (4:1) buffer solution was quenched by 25% with only 3.3 equivalents of PA, and was decreased by 95% with 50 equivalents of PA. The LOD was found to be 0.0578 μM. Metal ions, anions, and other nitroaromatics did not produce the same quenching phenomena as PA. The significant spectral overlap and insignificant lifetime change revealed the quenching mechanism to be the inner filter effect (IFE). Along with the IFE, the PET from polymer **18** to PA induced by acid–base interaction was also responsible for the quenching. The probe was able to detect PA in natural water samples, as well as on probe-**18**-coated test strips.

1

2

3

4

5a R = Imid R₁ = H
5b R = CH₃, R₁ = H
5c R = CH₃, R₁ = CH₃

6

7

8

9

10a R₁ = R₂ = H
10b R₁ = H, R₂ = CH₃
10c R₁ = R₂ = CH₃
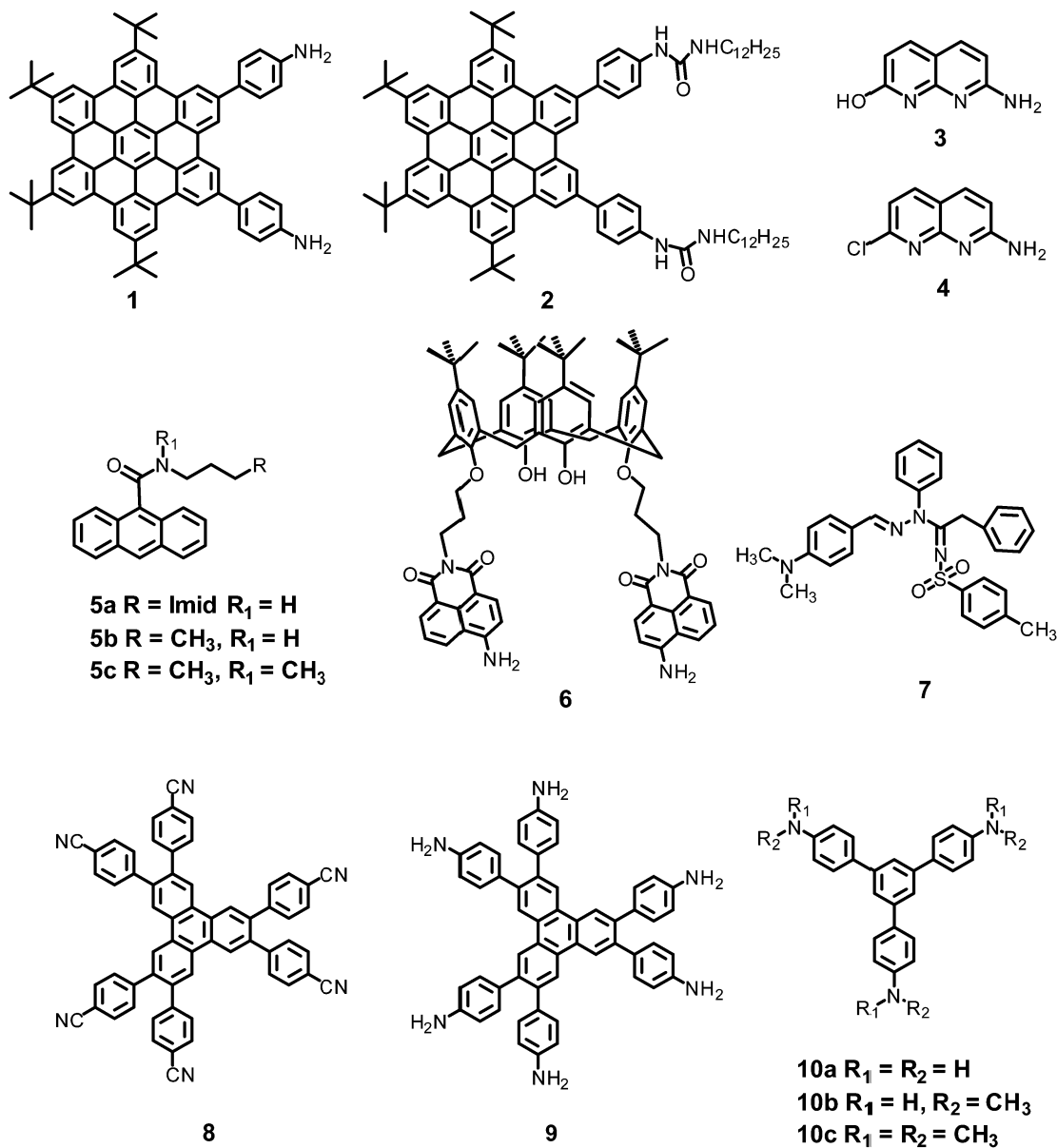
Chart 2   Structures of probes **1–10**.

11

12

13

14

15

16

17
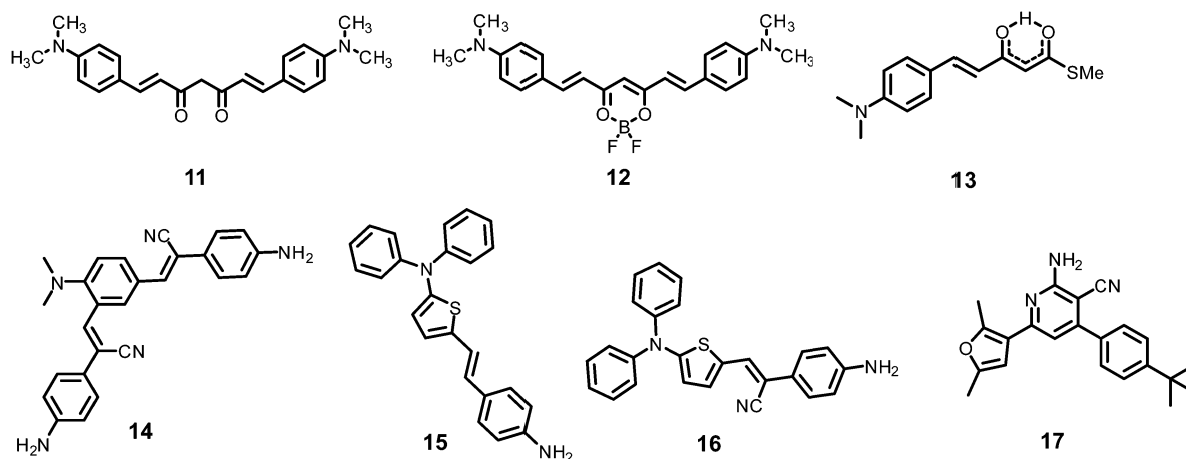
Chart 3   Structures of probes **11–17**.
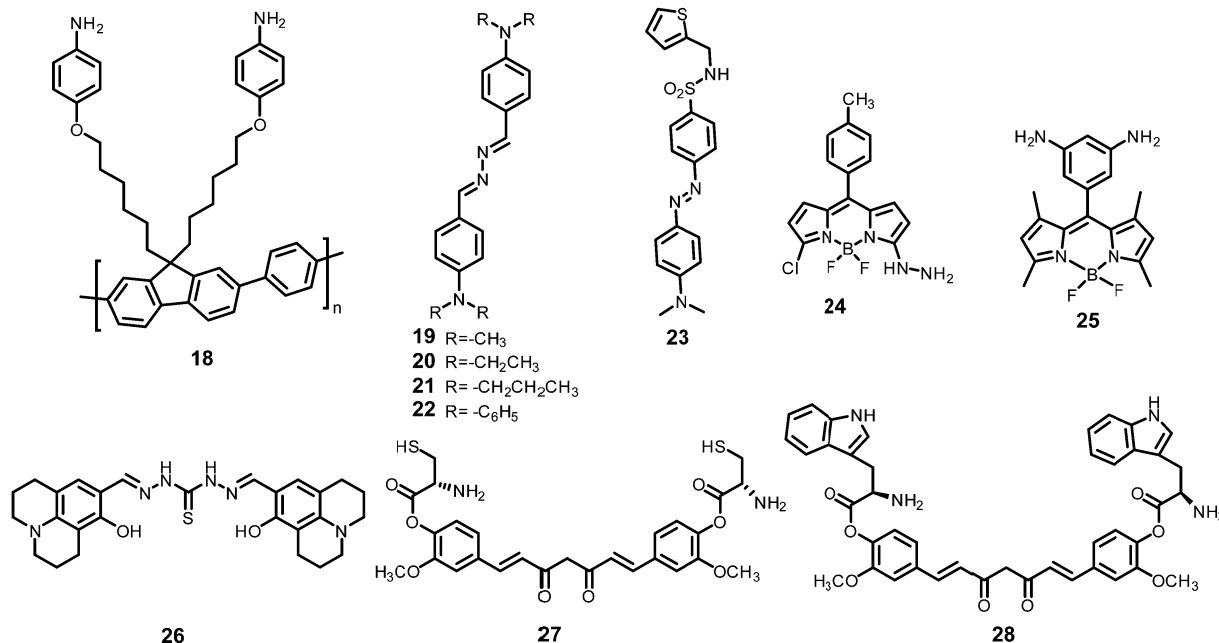
Chart 4   Structures of probes **18–28**.
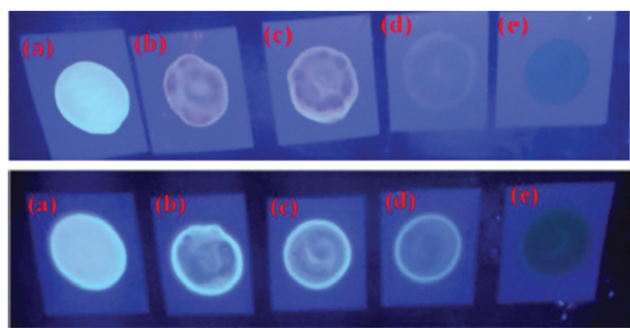
Fig. 1 Fluorescence images of TLC plates coated with probe **3** (upper) and probe **4** (lower) with various amounts of PA: (a) 0 M; (b) 10^{-5} M; (c) 10^{-4} M; (d) 10^{-3} M; and (e) 10^{-2} M. Reprinted from ref. 34, Copyright 2015 Royal Society of Chemistry.
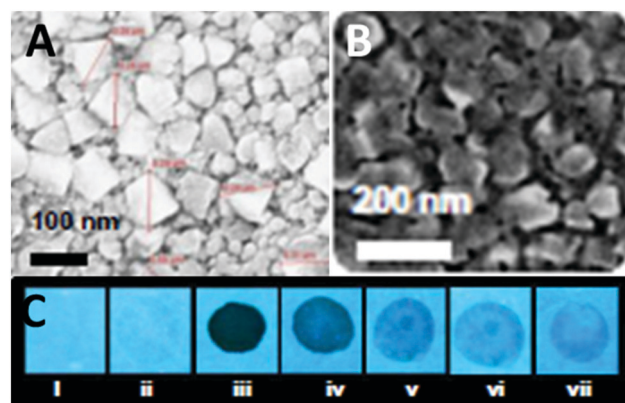
Fig. 3 Scanning electron microscopy (SEM) images of (A) **9** in a H_2O–THF (1:1) mixture and (B) **9** in a H_2O : THF (7:3) mixture. (C) Photographs of paper strips coated with **9** showing fluorescence quenching (under 365 nm light): (i) blank paper strip and (ii) paper strip with a drop of water; paper strips upon the addition of 10 μl of solutions of PA with different concentrations: (iii) 10^{-3} M, (iv) 10^{-5} M, (v) 10^{-7} M, (vi) 10^{-9} M, and (vii) 10^{-11} M. Reprinted from ref. 38, Copyright 2015 Royal Society of Chemistry.
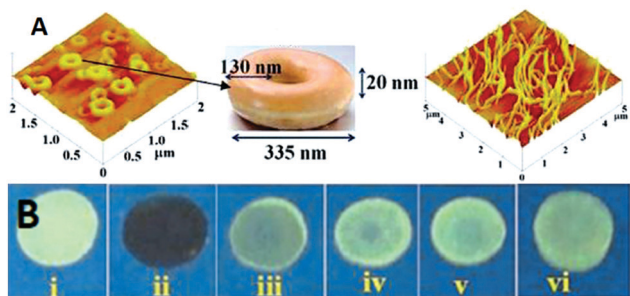
Fig. 2 (A) The donut-like structure of **6** transformed into ribbon-like fibrils upon treatment with PA. (B) Fluorescence quenching of **6** at different concentrations of PA: (i) only **6**; (ii–vi) {**6** + PA}: (ii) 100 mm, (iii) 10 mm, (iv) 1 mm, (v) 100 nm, and (vi) 10 nm. Reprinted from ref. 36, Copyright 2015 Wiley Online.

AIE-based azine derivatives **19–22**[49] (Chart 4) exhibited the appearance of a new absorption band with PA in THF. In the presence of PA, probe **19** displayed decreased absorption at 380 nm and the appearance of a new maximum at 480 nm with an isosbestic point at 415 nm and a colour change from colourless to yellow. Upon excitation at 415 nm, **19** displayed a gradual increase in fluorescence intensity at its emission maximum (576 nm) with increasing concentration of PA. Other NACs, such as 2-NP, 3-NP, 4-NP, 2,4-dinitrobenzoic acid and NB, did not induce any such change in the absorption and emission of the azine derivative in THF. This highly selective increase in fluorescence intensity by PA could be assigned to the formation of H-bonding between PA and the nitrogen of the
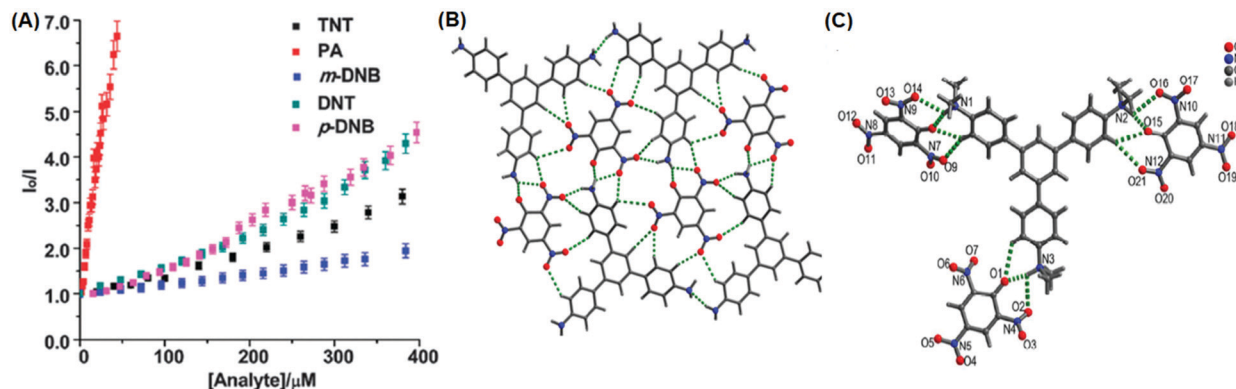
Fig. 4 (A) Stern–Volmer plots of the fluorescence quenching of **10a** (1.0 mM in acetonitrile) with TNT, PA, *m*-DNB, DNT, and *p*-DNB. (B) The crystal structure of the **10a**(PA) complex showing hydrogen bonds. (C) The crystal structure of the **10c**(PA)$_3$ complex showing hydrogen bonds (H-bonds are shown as dashed bonds). Reprinted from ref. 39, Copyright 2014 Royal Society of Chemistry. Reprinted from ref. 40, Copyright 2014 American Chemical Society. Reprinted from ref. 41, Copyright 2015 Royal Society of Chemistry.
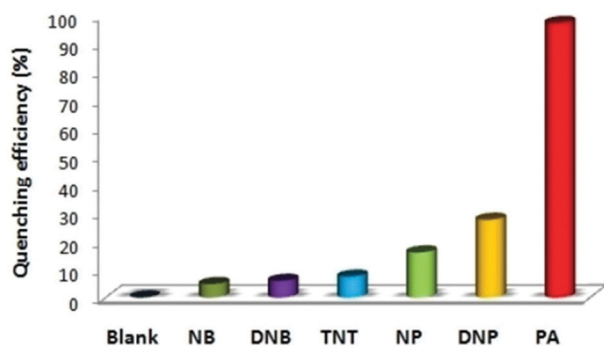
Fig. 5 Relative fluorescence quenching of **13** (10^{-5} M) in THF–H$_2$O (4 : 6) upon the addition of various NACs (30 equivalents). Reprinted from ref. 44, Copyright 2018 Wiley Online.
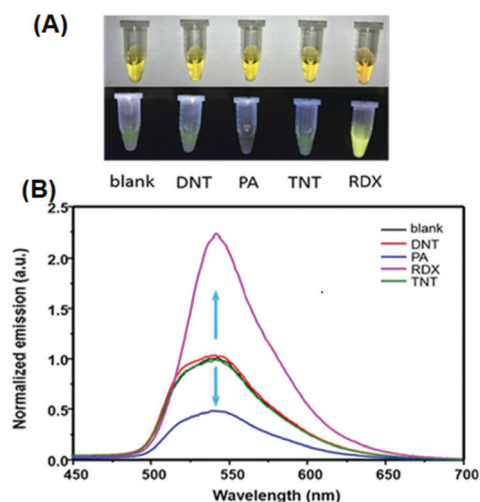
Fig. 6 (A) Images of the products after the reaction of different explosives with probe **24** in daylight (top) and under a 365 nm UV lamp (bottom). (B) Normalized emission spectra in the presence of different explosives. The concentration of the explosives is 40 μM, λ_{ex} = 365 nm, and λ_{em} = 540 nm. Reprinted from ref. 51, Copyright 2019 American Chemical Society.

N,*N*-dimethylamino moiety, resulting in increased internal charge transfer and the stabilization of the more-polarised excited state. In THF–H$_2$O (3 : 7), probe **19** exhibited a similar red-shift in the absorption band to 490 nm with PA due to ground-state complex formation, but displayed fluorescence quenching at 567 nm in fluorescence studies.

The addition of picric acid to probe **23**[50] (Chart 4) caused a shift in the absorption maximum from 440 nm to 500 nm and fluorescence quenching at 350 nm and 520 nm. The ^{1}H NMR spectrum of probe **23** with picric acid revealed the downfield shift of the –N(CH$_3$)$_2$ protons from δ 3.13 ppm to 3.25 ppm, as well as a shift in the aromatic protons of picric acid from δ 9.00 ppm to δ 9.10 ppm due to electrostatic and hydrogen-bond interactions.

Hydrazine-substituted BODIPY probe **24**[51] (Chart 4) displayed emission with a maximum at 540 nm in CH$_3$CN–water (8 : 2) and distinctly differentiated RDX and PA from each other and from other explosives through different absorption and fluorescence signals. 40 μM of 2,4-DNT, PA, TNT and RDX were tested, and only RDX caused the fluorescence enhancement of probe **24**, together with an obvious color change to bright yellow, while PA prominently decreased the fluorescence intensity (Fig. 6a). The fluorescence intensity of probe **24** declined linearly as the

concentration of PA was increased from 0 to 40 μM, and a quenching efficiency of 65.14% was obtained. In the case of RDX, the HCHO released from RDX formed a Schiff base with the hydrazine derivative to inhibit the PET process and resulted in a fluorescence enhancement (Fig. 6b). In case of PA, the inner-filter effect caused fluorescence quenching of fluorophore **24**.

The "turn-on" fluorescent BODIPY probe **25**[52] (Chart 4) revealed a 300-fold enhancement in emission intensity at 513 nm with 10 equivalents of PA in ethanol upon excitation at 499 nm. The Job's plot showed the formation of a 1 : 1 stoichiometric complex between probe **25** and PA. Therefore, only one of the two amino groups could be protonated by PA. The Benesi–Hildebrand plot gave a binding constant of 1.91×10^4 M^{-1}. Probe **25** could detect PA concentrations as low as 0.65 ppb.

Hydrazone-based probe **26**[53] (Chart 4) in DMSO–H$_2$O (1 : 4) exhibited intense green fluorescence centred at 496 nm due to
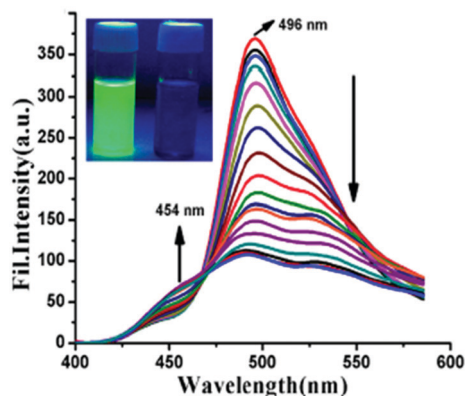
Fig. 7 Emission spectra of probe **26** (λ_{ex} = 367 nm) with PA (0–2 equiv.). The inset shows the fluorescence color change before (intense green) and after (low-intensity blue) the addition of PA to **26**. Reprinted from ref. 53, Copyright 2017 American Chemical Society.

an ESIPT process. With 2 equivalents of PA, the intensity of the probe at the 496 nm emission maximum decreased with the appearance of a new maximum at 454 nm (Fig. 7). This quenching behaviour was due to the hydrogen bonding inter-actions between PA and the basic amine NH of probe **26**, which resulted in inhibition of the ESIPT. The model compound *O*-methylated derivative of **26** was non-fluorescent and showed no interaction with PA. This proved the importance of the phenolic –OH group and the ESIPT mode for quenching. The quenching effect was found to be rapid (response time <1 min), selective, and pH independent. Furthermore, probe **26** was used to detect PA in the solid and vapor state, and in real water samples.

The two curcumin-based probes **27** and **28**[54] (Chart 4) were synthesized by linking curcumin with L-cysteine in probe **27** and L-tryptophan in probe **28**. These probes bind with PA due to the presence of basic amine groups. The weak emission bands at 540 nm and 535 nm for **27** and **28**, respectively, were enhanced 26.5-fold after the addition of 70 nM PA. The electro-static interactions of the protonated fluorophore with the picrate anion caused strong association and aggregation, which were responsible for the fluorescence enhancement. The probes had high selectivity, low interference, and a quick response. Practical applications for sensing PA in the solid state and in real water samples were also studied.

2.2 Protonation of pyridine-based fluorescent probes for picric acid

In general, picric acid can form a hydrogen bond with a pyridine nitrogen to stabilize the hydrogen-bonded complex or can completely transfer the proton to the pyridine nitrogen to form an ionic complex. These situations differ only in the extent of internal charge transfer. The fluorescent probes **29–60** (Charts 5–7) protonate the pyridine nitrogen, and a comparison of the solvents, LODs, K_{SV} values, emission maxima and applications of probes **29–60** has been presented in Table 2.

The AIEE-active mono-, di- and tetra-pyridine-substituted pentacenequinone-based probes **29a–29c**[55] (Chart 5) exhibited increased fluorescence intensity upon increasing the water fraction or viscosity and decreasing the temperature due to restriction in rotation (RIR). In DMSO–H$_2$O (1:1) mixtures, probes **29a**, **29b** and **29c** showed >95% fluorescence quenching
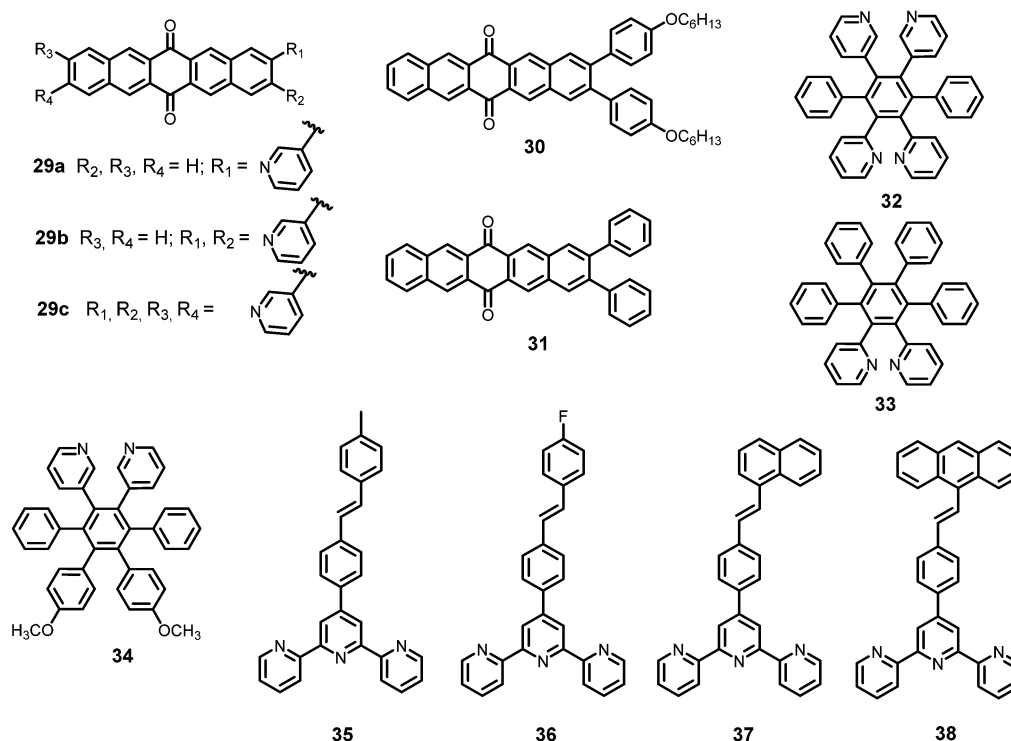
Chart 5 Structures of probes **29–38**.
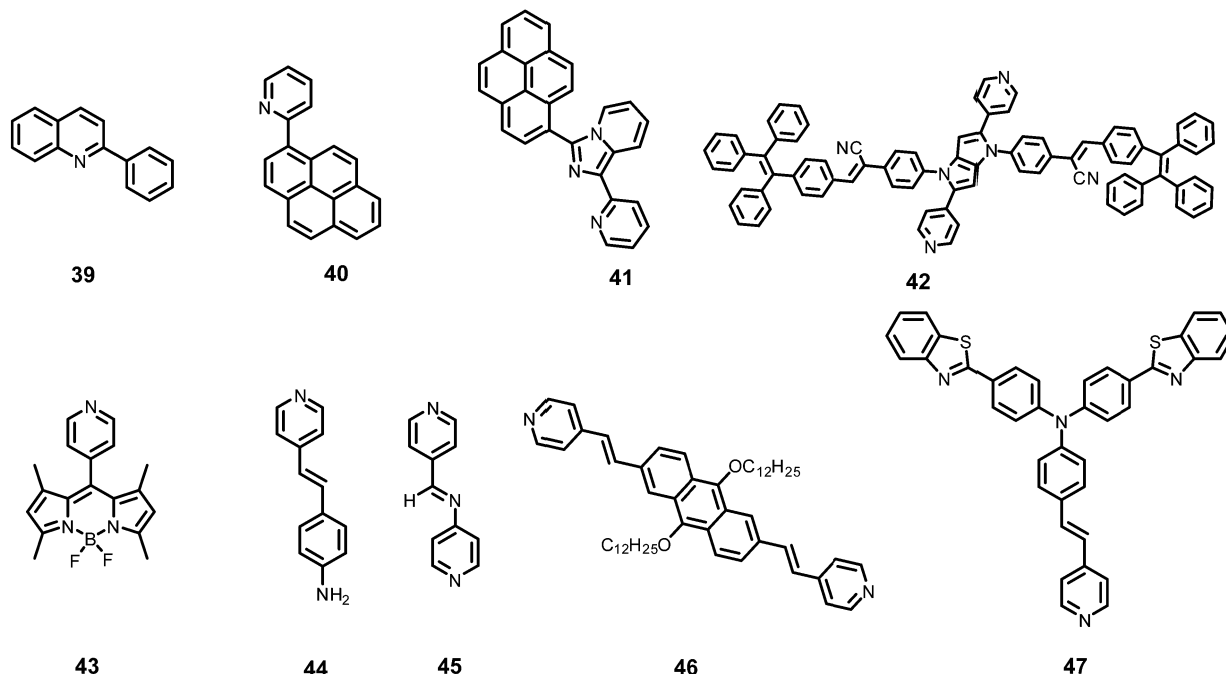
Chart 6 Structures of probes **39–47**.
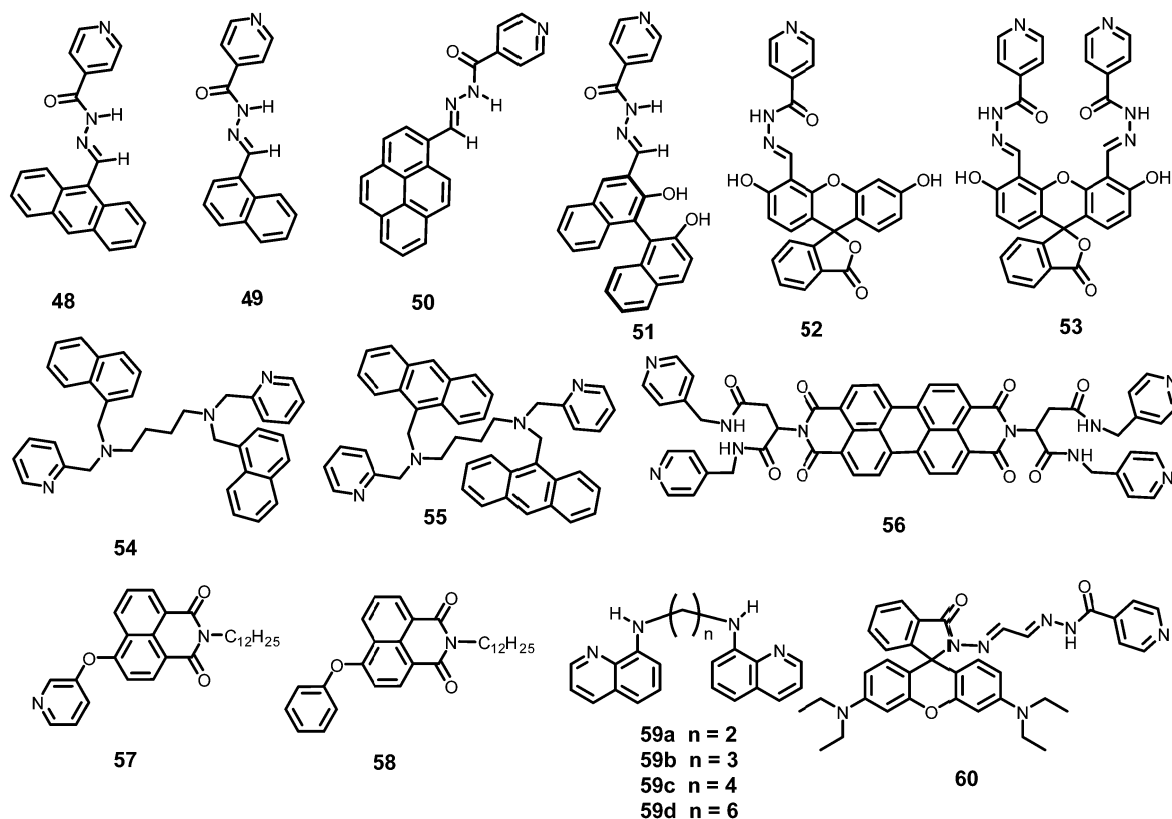
Chart 7 Structures of probes **48–60**.

with 62, 60 and 58 equivalents of PA, respectively. The fluorescence quenching by PA was attributed to electron and/or energy transfer mechanisms.

The minimum detection limit for PA was 600 nM with probe **29c**. Probes **29a–29c** were non-selective towards PA, and other NACs such as TNT, 2,4-DNT, 1,3-DNB, and DNBA also caused

competitive fluorescence quenching in these probes. Probes **30–31** showed similar results with PA and other NACs. TLC strips coated with **29c** could detect 10^{-8} M PA *via* fluorescence quenching.

Among the hetero-oligophenylene derivatives **32–34**,[56] (Chart 5), derivative **32** bearing four 3-pyridyl moieties exhibited quenching of its fluorescence intensity at an emission maximum of 339 nm with 2.5 equivalents of PA, but with >2.5 equivalents of PA, a new emission band appeared at 446 nm. Its intensity increased gradually with increasing amounts of PA and was finally red-shifted to 460 nm (Fig. 8A and B). The π–π interactions of derivative **32** with PA probably caused the fluorescence quenching at 339 nm, and at higher amounts of PA, the excited-state intermolecular proton transfer from PA to the pyridyl nitrogen resulted in the new emission band at 460 nm. Derivative **33** with 2-pyridyl groups exhibited similar results with PA, but derivative **34** exhibited only fluorescence quenching. Paper strips (Fig. 8C) coated with **32** could detect 10^{-12} M PA.

The extended π-conjugated arylene–vinylene probes **35–38**[57] (Chart 5) displayed a gradual red-shift of their emission maximum from 417 (in the case of **35**) to 498 nm (in the case of **38**). The maximum quantum yield and red-shift of the emission for probe **38** were found to be due to anthracene having the maximum π-conjugation and minimum HOMO–LUMO energy gap. The intensity of the emission for all four probes in chloroform solution decreased after the addition of PA, but there was no interference

Fig. 9 The visual detection of different concentrations of PA using paper test strips coated with probe **38**, demonstrating its remarkable sensitivity towards trace PA down to the nanomolar level. Reprinted from ref. 57, Copyright 2017 Royal Society of Chemistry.

from any other nitroaromatics, such as NB, NT, 4-NP, 4-NB acid, or 2,4-DNT. With PA, the colour of the probe **38** solution turned an intense yellow owing to the formation of a charge-transfer complex with PA. Moreover, the spectral overlap of the absorption with the emission bands of the probes permitted energy transfer from the excited state of the arylene–vinylene unit of probes **35–38** to the ground state of PA and increased the fluorescence quenching efficiency. Paper strips (Fig. 9) coated with probe **38** could detect 10^{-9} M PA from 5 μl of solution.

The small molecule phenyl quinoline (**39**)[58] (Chart 6) emits weakly at 359 nm in THF, but the addition of 90% water (SDS – 4 mM) resulted in an increase in the fluorescence intensity and quantum yield due to the formation of rod-like microstructures (Fig. 10). The addition of PA resulted in 80% quenching of the fluorescence intensity *via* a static quenching mechanism with no change in the emission maximum, whereas the other NACs exhibited lower fluorescence quenching, *viz.* 4-NP (34%), 2,4-DNP (15%), NA (12%), DNT (5%) and DNB (3%). Probe **39** was also used as an acid–base sensor due to its ratiometric fluorescence emission in presence of acids and bases.

Probe **40**[59] (Chart 6) in methanol with PA displayed a linear relationship between the ratio of the emission intensities (I_{522}/I_{405}) and the concentration of PA in the range of 5–100 μM. In the ^{1}H NMR spectrum of the probe–PA in CDCl$_3$, the up-field shift of the OH signal of picric acid from δ 9.23 ppm to 8.56 ppm and the down-field shift of the pyridine protons supported the formation of a ground state charge transfer complex, and the overlap of the emission of probe with the absorption spectrum of PA supported a FRET process.

Fig. 8 (A) Fluorescence spectra of **32** (50 μM) with picric acid (125 μM) in H$_2$O–EtOH (6 : 4) in HEPES, pH = 7.0; λ_{ex} = 273 nm. (B) Fluorescence spectra of **32** (50 μM) with 350 μM of PA in H$_2$O–EtOH (6 : 4); λ_{ex} = 273 nm. (C) Photographs of **32**-coated TLC strips under different experimental conditions: (i) (a) PA crystals on top of TLC strips coated with derivative **32** and (b) the removal of the PA crystal after 5 s; (ii) photographs of the fluorescence quenching of **32**-coated TLC strips by PA, DNT, and TNT in contact mode (10 μL of analyte with a contact area of 0.05 cm^2). Reprinted from ref. 56, Copyright 2014 Royal Society of Chemistry.

Fig. 10 SEM images of probe **39** with 4 mM SDS. Reprinted from ref. 58, Copyright 2018 Royal Society of Chemistry.
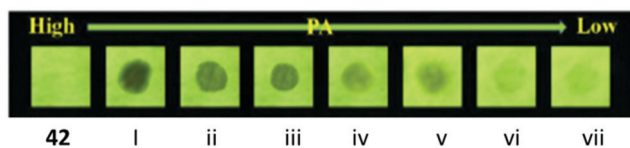
Fig. 11 Photographs of the fluorescence quenching of probe **42** for detecting different concentrations of PA. From left to right: blank, (i) 5.0×10^{-3} M, (ii) 1.0×10^{-3} M, (iii) 5.0×10^{-4} M, (iv) 1.0×10^{-4} M, (v) 5.0×10^{-5} M, (vi) 1.0×10^{-5} M. Reprinted from ref. 61, Copyright 2019 Elsevier.

Pyrene-tethered probe **41**[60] (Chart 6) exhibited an emission maximum at 495 nm in THF, which gradually shifted to 515 nm with increasing amounts of DMF in THF–DMF binary mixtures and demonstrated the occurrence of an ICT transition in probe **41**. A solution of probe **41** in DMSO displayed efficient fluorescence quenching at an emission maximum of 530 nm by PA. Among other nitroaromatics, only 2,4-DNP showed some interference. Theoretical studies clearly indicated that the pyridine nitrogen preferably formed a hydrogen bond with the OH group of PA and was primarily responsible for the fluorescence quenching. Probe **41** could also detect PA in a 50% DMSO–water medium. A portable fluorimeter module interfaced wirelessly with a smartphone could detect 99 nM PA.

TPE- and pyridine-unit-based probe **42**[61] (Chart 6) revealed strong AIE behaviour with a strong green emission maximum at 527 nm in a DMF–water (1:99) mixture. These aggregates of probe **42**[61] with PA exhibited fluorescence quenching at 527 nm with a color change from yellow to dark with an LOD of 31.5 nM. ^{1}H NMR and DFT studies clearly indicated that the protonation of the pyridine nitrogen by the OH group of PA followed by PET from the fluorophore to PA was primarily responsible for the fluorescence quenching. Paper strips coated with probe **42** detected 10^{-5} M of PA (Fig. 11).

Upon excitation at 375 nm, p-pyridine BODIPY probe **43**[62] (Chart 6) showed a 95.8% decrease in the emission intensity at 522 nm with 2 equivalents of picric acid in DMSO–H_2O (1:1). The bright green fluorescence color of probe **43** changed to dark in 30 s due to the protonation of the pyridine nitrogen followed by PET from the excited-state probe to the ground-state PA. The Stern–Volmer constant (K_{SV}) of the probe was calculated to be 7.69×10^4 mol L^{-1}, and it could detect PA concentrations as low as 0.013 μM.

Pyridine-based probe **44**[63] (Chart 6) in THF displayed the formation of a new absorption maximum at 424 nm with PA with a color change from colorless to yellow. Probe **44** showed an 87% reduction in fluorescence intensity at 440 nm with 1 equivalent of picric acid, and with higher amounts of PA, a new emission band with weak emission appeared at 550 nm. The appearance of the new emission band could be assigned to the increased ICT upon protonation at the pyridine nitrogen, which is supported by the X-ray crystal structure in the solid state. The K_{SV} and LOD were calculated to be 4.106×10^5 M^{-1} and 400 ppb, respectively.

Probe **45**[64] (Chart 6) in CH_3CN–HEPES buffer (4:1) exhibited fluorescence quenching with a gradual shift in the emission maximum from 410 nm to 460 nm as the amount of PA was increased to 2.0 equivalents. These results, along with Job's plot and DFT-DT studies, suggest that two molecules of PA bind with one molecule of probe **45** and cause fluorescence quenching through a combination of ICT and FRET mechanisms. A lightweight, convenient and portable prototype for PA detection was also fabricated.

Probe **46**[65] (Chart 6) revealed intense emission at 500 nm in THF, which vanished (94%) with 100 equivalents of PA. In the fluorescence spectrum of probe **46**, the presence of the shoulder at 625 nm with higher equivalents of PA indicated the presence of charge-transfer character. Other nitro-phenols also induced significant fluorescence quenching of probe **46** at higher concentrations (Fig. 12A). Based on studies of the dynamic quenching mechanism of **46** by PA, the X-ray crystal structure of the **46** ∩ PA complex and titrations, the combined effect of the proton-induced ICT in **46** and electron transfer from the electron-rich anthracene to the electron-deficient PA moiety was assigned as the cause of the fluorescence quenching. Moreover, a human thumb impression (Fig. 12B) was clearly visible on a test strip coated with probe **46**.

Triphenylamine-based probe **47**[66] (Chart 6) having two benzothiazole moieties and one vinyl pyridine moiety at its 1,
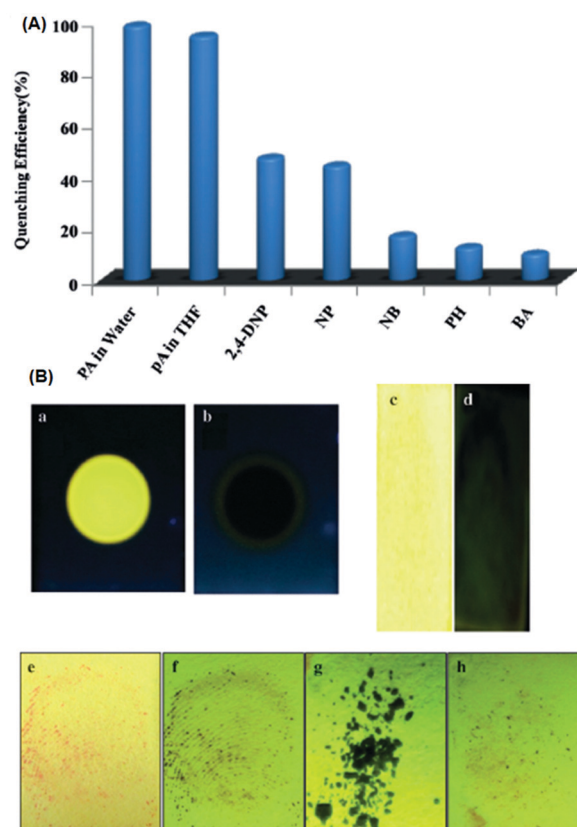
Fig. 12 (A) Fluorescence quenching efficiency of **46** towards different analytes. (B) Images of a **46**-coated TLC plate under UV light (a) before and (b) after the addition of PA. Images of test strips consisting of **46**-coated Whatman Filter (c) before and (d) after being dipped into aqueous solutions of PA. Thumb impressions with PA on a test strip under (e) normal light and (f) UV light. (g) PA crystals on top of a test strip for 5 min, and the strip after the removal of the PA crystals. Reprinted from ref. 65, Copyright 2016 Wiley Online.

3 and 5 positions underwent fluorescence quenching at 500 nm with a decrease in quantum yield from 0.31 to 0.08 with one equivalent of PA in a methanol–water (8:2) mixture. The protonation of the pyridine nitrogen associated with ICT was mainly responsible for the formation of a 1:1 stoichiometric non-fluorescent complex. The LOD was found to be 100.4 µM. Probe **47** was also used for the detection of Fe^{3+} ions.

N-Acylhydrazone **48**[67] (Chart 7) displayed an excimer emission band at 483 nm (λ_{ex} = 419 nm), which underwent a 97% decrease in fluorescence intensity with 3 equivalents of PA in DMF. An ethanolic solution of **48** with 1 equivalent of PA gave vermilion precipitates (Fig. 13). None of the other tested NACs, *viz.* TNT, 2,6-DNT, NB, 4-NP, 1,3-DNB and NBA, caused fluorescence quenching or resulted in the formation of precipitates. The down-field shift of the protons of pyridine in the ^{1}H NMR titration of **48** with PA pointed to proton transfer from PA to the pyridine nitrogen. The X-ray crystal structure of the **48** ∩ PA complex confirmed the proton transfer to pyridine nitrogen and the formation of a supramolecular complex through multiple hydrogen-bond and π–π interactions.

Extending this work, these authors synthesized three additional *N*-acylhydrazone[68]-based probes, **49–51**, for PA detection. Among probes **49–51**, probe **50** with a pyrene moiety as the fluorophore exhibited the greatest fluorescence quenching with PA and had the highest Stern–Volmer constant (5.12×10^6 M^{-1}) and lowest detection limit (0.102 µM). Their host–guest interactions were studied using ^{1}H NMR titration and X-ray structural studies and revealed the formation of 1:1 host–guest complexes through multiple hydrogen-bond interactions in solution and in the solid state.

Fluorescein-based chemosensors **52** and **53**[69] (Chart 7) (20 equivalents) in ethanol or water (buffer) solution with PA revealed fluorescence quenching at 545 nm and 558 nm upon excitation at 500 nm. The K_{sv} values and detection limits of probes **52** and **53** in ethanol were better than those observed in buffer. Probes **52** and **53** displayed fluorescence quenching with PA due to H-bonding and electron transfer. Paper strips coated with **52** and **53** could detect PA concentrations down to 10^{-6} M from a droplet (Fig. 14).

Pyridine-based fluorescent sensors **54** and **55**[70] (Chart 7) displayed fluorescence quenching at 420 nm and 450 nm with PA, respectively. Both probes **54** and **55** displayed similar fluorescence quenching efficiency (Fig. 15A) by PA (98% for **54** and 90% for **55**), but probe **54** exhibited higher selectivity towards PA over other NACs than that observed for probe **55**.

Fig. 14 Paper strips for the visual detection of different concentrations of PA under visible and UV light. [PA] = 0 mM, 10.0 mM, 1.0 mM, 8.0 × 10^{-1} mM, 6.0 × 10^{-1} mM, 4.0 × 10^{-1} mM, 2.0 × 10^{-1} mM, 1.0 × 10^{-1} mM, 1.0 × 10^{-2} mM, and 1.0 × 10^{-3} mM. Reprinted from ref. 69, Copyright 2017 Royal Society of Chemistry.
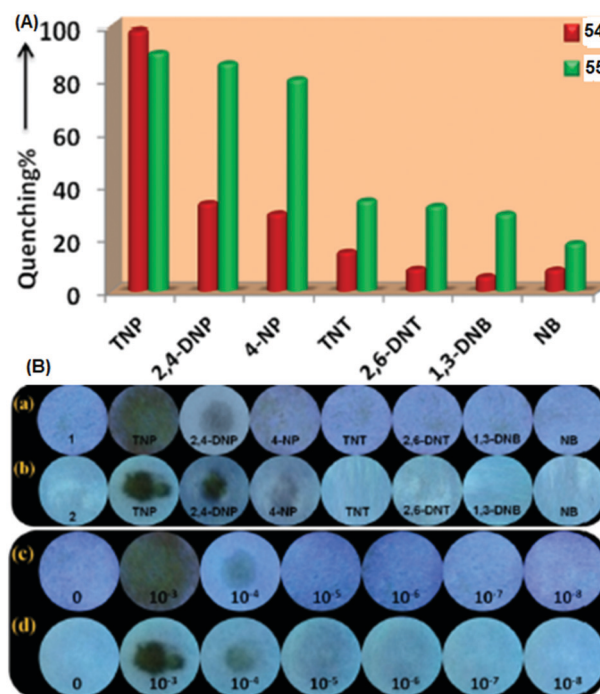
Fig. 15 (A) A comparison of the percent quenching of **54** and **55** with different NACs. (B) Photographs of test paper strips coated with (a) **54** and (b) **55** and their responses towards NACs. Photographs of paper strips coated with (c) **54** and (d) **55** for the visual detection of increasing amounts of PA (10^{-8} to 10^{-3} M). Reprinted from ref. 70, Copyright 2018 American Chemical Society.

Fig. 13 Photographs of solid **48** and its complex **48** ∩ PA. Reprinted from ref. 67, Copyright 2011, Royal Society of Chemistry.

The smaller size of the naphthalene moiety in probe **55** resulted in less steric bulk than the anthracene moiety of **54** and provided space to allow for π–π interactions with PA, 2,4-DNP and 4-NP with equal ease. Based on ^{1}H NMR and DFT studies, hydrogen bonding between the pyridine nitrogen and OH group of PA and energy transfer *via* π–π interactions were proposed as mechanisms. The K_{SV} values for PA were 5.78 × 10^4 for probe **54** and 3.26 × 10^4 for probe **55**. Filter paper strips coated with aqueous suspensions of **54** and **55** detected PA concentrations as low as 10^{-8} M (Fig. 15B).

Perylenediimide–pyridine conjugate **56**[71] (Chart 7) displayed red-shifts in its absorption maxima from 488/523 nm to 493/529 nm and decreased fluorescence intensity due to proton

transfer from picric acid to probe **56**. The K_{SV} and LOD were found to be 6.87×10^4 M^{-1} and 0.0056 μM, respectively. Job's plot and ^{1}H NMR titration analyses revealed the protonation of all four pyridine nitrogen atoms with four molecules of picric acid and the formation of a 1:4 complex between probe **56** and picric acid.

Probe **57**[72] (Chart 7) in CH$_3$CN–H$_2$O (1:1) and probe **58**[72] in CH$_3$CN formed an organo-gel with an intertwined fiber network at critical gelation concentrations of 0.69 w/v% and 0.45 w/v%, respectively. The organo-gel prepared from probe **57** was more sensitive than that prepared from probe **58** towards PA and could also extract PA from the aqueous solution into the organogel system. The 16 nm blue-shift of the fluorescence emission band of the gel of **57** at 501 nm with PA pointed to the suppression of the TICT excited state of **57**. Probe **57** displayed greater fluorescence quenching than probe **58** with PA (1 equiv.) due to the H-bonding between the pyridine nitrogen and OH of PA. The protons of the pyridine group in probe **57** shifted downfield in the ^{1}H NMR titration with PA. Paper strips (Fig. 16) coated with probe **57** showed a change in fluorescence from blue to non-fluorescent.

Quinoline-based probes **59a–59d**[73] (Chart 7) showed fluorescence quenching of 86–88% upon excitation at 335 nm due to ground-state complexation between the probe and PA. The downfield shift of the quinoline protons in the ^{1}H NMR spectra of these probes upon the addition of picric acid and Job's plot analysis confirmed the protonation of the quinoline nitrogen and the formation of 1:2 stoichiometric complexes with the picrate anion.

The rhodamine–isonicotinic hydrazide-based "turn-on" fluorescent probe **60**[74] (Chart 7) showed selective detection of PA in CH$_3$CN–H$_2$O (1:9) through a spirolactam ring-opening process. Probe **60** underwent protonation by PA at the pyridine nitrogen and displayed a new absorption maximum at 559 nm with a color change from colourless to pink and enhancement of the emission intensity at 581 nm. A Job's plot analysis revealed a 1:1 stoichiometry between probe **60** and PA with a binding constant of 6.4×10^7 M^{-1}. Probe **60** could detect PA concentrations as low as 0.0373 μM. Colourless paper strips (Fig. 17) coated with probe **60** became pink when exposed to PA.
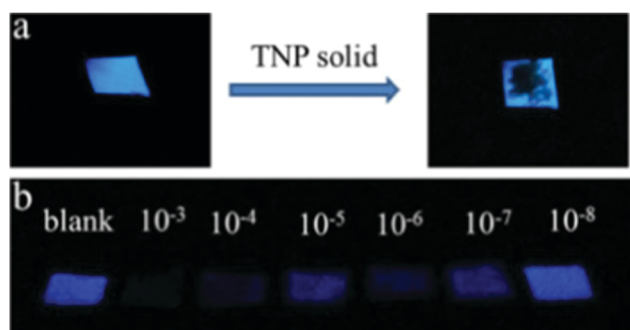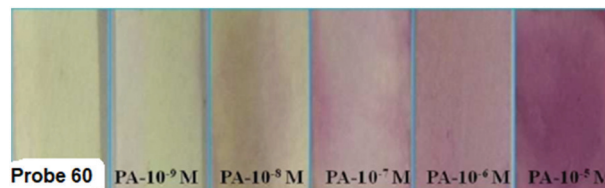
Fig. 17 Photographs of probe **60** on test strips, showing the colour changes for the visual detection of PA. Reprinted from ref. 74, Copyright Wiley Online.

2.3 Protonation of imidazole-based fluorescent probes for picric acid

Probes **61–72** undergo protonation by picric acid at the imidazole nitrogen to form imidazolium salts, and in each case, quenching of the fluorescence intensity is observed. A comparison of the solvents, LOD, K_{SV} values, emission maxima and applications of probes **61–72** has been given in Table 3.

Imidazole-based probe **61**[75] (Chart 8) displayed 95.3% fluorescence quenching at 392 nm (Fig. 18) in DMSO–H$_2$O (7:3), and probe **62** underwent 92.4% fluorescence quenching at 345 nm in EtOH–H$_2$O (7:3) with 12 equivalents of PA, whereas the other NACs induced insignificant changes in the fluorescence intensity of probes **61** and **62**. In their ^{1}H NMR spectra, the imidazole NH signals of **61** and **62** disappeared upon the interaction of PA with the probe. Probes **61** and **62** formed 1:2 and 1:1 stoichiometric complexes with PA, respectively. Probes **61** and **62** detected PA concentrations as low as 0.17 μM and 0.49 μM.

Probes **63–65**[76] (Chart 8) displayed blue emission maxima between 400–413 nm, which were selectively quenched by PA in a DMSO–H$_2$O (1:9) mixture. These derivatives formed GSCT complexes with PA owing to the protonation of the imidazole nitrogen, and the increased efficiency of PET and IFE caused faster fluorescence quenching. Probe **63**, due to the additional hydrogen bonding interaction of the OH of the probe with picric acid, exhibited higher-efficiency fluorescence quenching by PA than that observed for probes **64** and **65**. Cyclic voltammetry studies showed electron transfer from the high-energy LUMO of the photo-excited probe to the low-energy LUMO of PA. These probes were able to detect PA from real samples. Paper strips coated with these probes could detect PA *via* fluorescence quenching.

The phenanthroline based probes **66a–66c**[77] (Chart 8) exhibited emission maxima at 386 nm, 486 nm and 456 nm, respectively. Solutions of these probes in ethanol showed fluorescence quenching with picric acid with respective limits of detection of 2.8 μM, 2.3 μM and 4.6 μM. The X-ray crystal structures of complexes of **66a** and **66c** with picric acid clearly show the transfer of the proton from picric acid to the phenanthroline nitrogen to form an ionic complex. The lack of change in the fluorescence lifetimes of these probes with picric acid further indicated that the existence of electrostatic interactions between the protonated probe and the picrate ion followed by PET was mainly responsible for the fluorescence quenching of probes **66** with picric acid.
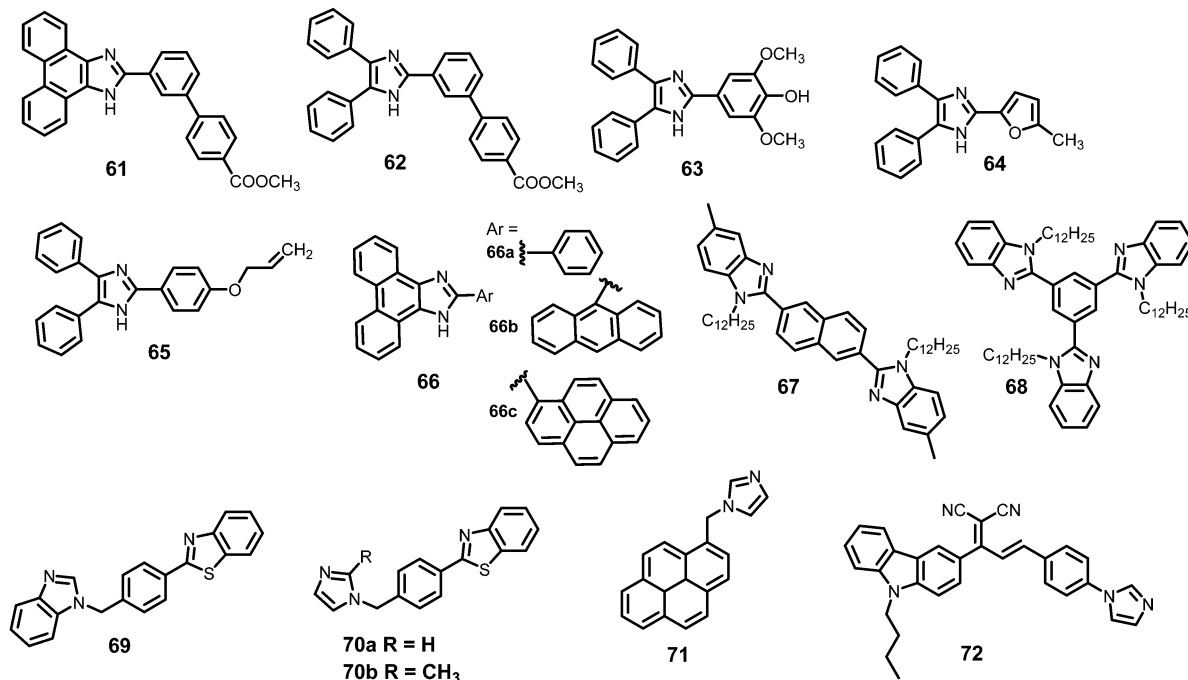

Fig. 16 Photographs of paper strips coated with probe **57** under a UV lamp (365 nm) for the visual detection of PA: (a) solid PA and (b) dropped PA solutions with different concentrations (M L^{-1}). Reprinted from ref. 72, Copyright 2017 American Chemical Society.

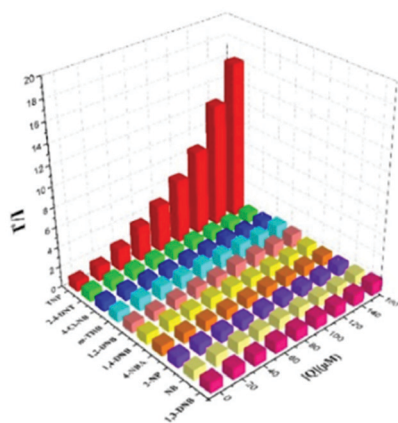**Chart 8** Structures of probes **61–72**.

Fig. 18 Change in the fluorescence intensity of probe **61** with various NACs. Reprinted from ref. 75, Copyright 2019 Elsevier.

Probe **67**[78] (Chart 8) with two benzimidazole moieties linked at the 2- and 6-positions of the naphthalene and long hydrophobic alkyl chains at the benzimidazole nitrogen self-assembled in water to form rod-like structures (Fig. 19), which
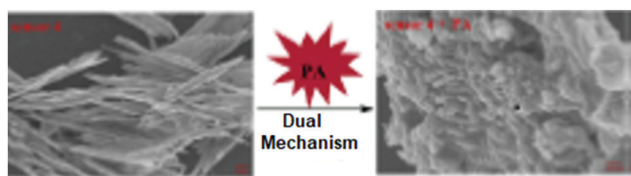

Fig. 19 The rod-like self-assemblies of probe **67** undergo a morphological change in the presence of two equivalents of PA (SEM images). Reprinted from ref. 78, Copyright 2017 Elsevier.

were disrupted by PA. A solution of probe **67** displayed an emission band at 422 nm, which was completely quenched by 5 equivalents of PA. GSCT complex formation *via* the picric-acid-mediated protonation of the benzimidazole nitrogen followed by efficient electron transfer from the fluorophore to picric acid are responsible for the fluorescence quenching. Probe **67** can detect PA from both the solution phase (LOD 0.0025 μM) and the solid-state *via* a contact mode (11.46 ag cm^2).

Among a series of benzimadazole-based tripodal derivatives, probe **68**[79] (Chart 8) with a $C_{12}H_{25}$ alkyl chain exhibited detection of picric acid (Fig. 20) both in solution and the solid phase with a detection limit of 0.218 μM. Chain lengths longer or shorter than C12 reduced the sensitivity of the probe towards picric acid. The fluorescence intensity enhancement of probe **68** was due to the protonation of the benzimidazole nitrogen with benzoic acid. In the case of picric acid and 2,4-DNP, the electrostatic interactions between protonated **68** and the picrate/2,4-dinitrophenolate anions caused efficient
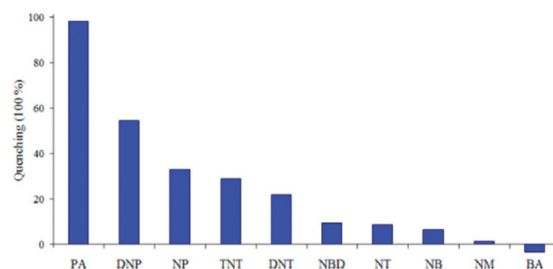
Fig. 20 The effects of different NACs on the fluorescence quenching of probe **68**. Reprinted from ref. 79, Copyright 2014 American Chemical Society.

energy transfer from the photoexcited π-electron-rich **68** to the ground state of electron-deficient PA, resulting in fluorescence quenching.

Probe **69**[80] (CHCl₃) with one equivalent PA and probe **70**[80] (Chart 8) with two equivalents of PA displayed >90% fluorescence quenching of the fluorescence at ∼367 nm, along with a red-shift of the maxima to 381 nm. Probe **69** formed a 1:1 (probe:picric acid) stoichiometric complex, while probe **70** formed a 1:2 stoichiometric complex. ¹H NMR, Job's plot and absorbance studies revealed that in the case of **70**, both the imidazole and benzothiazole nitrogen atoms are protonated by two molecules of picric acid to form a GSCT complex. Other NACs, such as DNT and 2,4-DNP, also induced significant quenching of the fluorescence of probes **69** and **70** (Fig. 21).

Paper strips coated with **70** turned from fluorescent blue to non-fluorescent (under 365 nm light) with 1 mM PA.

Probe **71**[81] (Chart 8) displayed both ON–OFF and OFF–ON fluorescence behaviour with picric acid, depending on the solvent. In CH₃CN, **71** displayed OFF–ON behaviour, but exhibited ON–OFF fluorescence quenching upon PA binding in toluene solution. In toluene, the fluorescence of probe **71** at 378 and 397 nm was quenched owing to GSCT complex formation and FRET from the fluorophore to picrate anion, and the detection limit for PA was 2.515 μM. However, in CH₃CN, the fluorescence intensity of **71** increased only 1.25-fold with a LOD of 1.065 μM for PA. The down-field shift of the imidazole and pyrene protons in the ¹H NMR spectrum of **71** pointed to protonation of the imidazole nitrogen and face-to-face π–π stacking interaction between the pyrene and picrate rings. Probe **71** formed two types (Fig. 22) of crystals with PA (space groups $P2_1/n$ and $P2_1/c$), and strong electrostatic interactions between the picrate anion and imidazolium moiety and π–π interactions between the pyrene ring and picrate anion were observed in the X-ray structures of both crystals.

Probe **72**[82] (Chart 8) gave an emission maximum of 460 nm in DMF, which was red-shifted to 574 nm in 90% water due to the formation of spherical aggregates with a diameter of

Fig. 22 X-ray crystal structures of complexes of probe **71** with PA showing π–π interactions between pyrene and the picrate anion. Reprinted from ref. 81, Copyright 2017 Elsevier.

233 nm. These aggregates showed 96% fluorescence quenching with 10 equivalents of picric acid and an LOD of 3.5 μM for picric acid. In the ¹H NMR spectrum of **72**, the C2–H of the imidazole moiety was shifted downfield by 1.39 ppm, which pointed to the formation of an imidazolium moiety via proton transfer from picric acid, and the resulting electrostatic interactions caused efficient PET from the fluorophore to the picrate anion to form a non-fluorescent complex.

2.4 Protonation of imine-based fluorescent probes for picric acid

The nitrogen in Schiff bases is basic in nature and is well known to undergo protonation with general acids, and accordingly, forms a salt with the nitrophenolate ions upon protonation by phenolic nitroaromatic compounds and facilitates electron transfer/energy transfer processes for efficient fluorescence quenching. A comparison of solvents, LOD, K_{SV} values, emission maxima and applications of probes **73–76** has been presented in Table 3.

Fluorescent probe **73**[83] (Chart 9) in CH₃CN with PA exhibited a blue-shift in its absorption band from 368 nm to 344 nm, and fluorescence quenching with a red-shift of the emission band
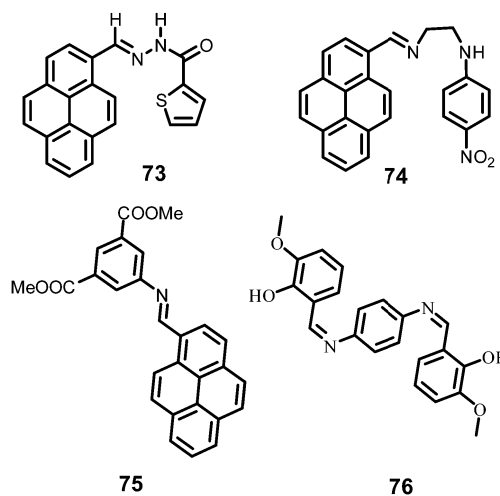

Fig. 21 The quenching efficiencies of different NACs toward probes **69** and **70**. Reprinted from ref. 80, Copyright 2019 Wiley Online.

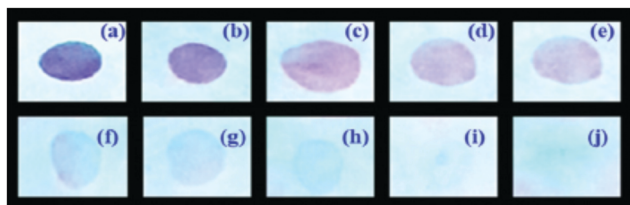Chart 9 Structures of probes **73–76**.

Fig. 23 Response of probe-**73**-coated paper strips to PA: (a) 10 μM, (b) 1.0 μM, (c) 0.1 μM, (d) 0.01 μM, (e) 8 nM, (f) 4 nM, (g) 1 nM, (h) 0.5 nM, (i) 0.1 nM, and (j) 0. Reprinted from ref. 83, Copyright 2019 Royal Society of Chemistry.

from 425 nm to 462 nm and a fluorescence color change from blue to dark. A Job's plot analysis showed a 1 : 1 stoichiometry with a binding constant of $6.814 \times 10^6 \, \text{M}^{-1}$. The protonation of the imine nitrogen followed by energy transfer from the probe to the picrate was responsible for the quenching of the emission intensity. The LOD and K_{SV} values are 0.01 μM and $2.29 \times 10^7 \, \text{M}^{-1}$ respectively. Probe **73** detected 10^{-9} M PA using paper strips (Fig. 23).

Probe **74**[84] (Chart 9) is AIEE-active, and upon the addition of 80% water to its solution in CH_3CN, displayed an 833-fold enchantment in fluorescence intensity and achieved a 0.79 quantum yield. Probe **74** with 24 equivalents of PA exhibited >98% fluorescence quenching at 476 nm with a change from a cyan-blue colour to non-fluorescence. Other phenolic NACs, such as 2,4-DNP and 4-NP (Fig. 24), also caused significant fluorescence quenching of probe **74**. Along with the probable protonation of amine nitrogen, the intercalation of the picric acid between two pyrene rings held together by π–π stacking interactions in the aggregated state contributed to a CT process from pyrene to picric acid.

Another pyrene-Schiff-base AIE fluorescent probe, **75**[85] (Chart 9), exhibited fluorescence quenching at 469 nm in THF–H_2O (1 : 9) with the gradual addition of PA due to ground-state energy transfer via π–π and coulombic interaction between the fluorescent probe and the picrate anion. The K_{SV} and detection
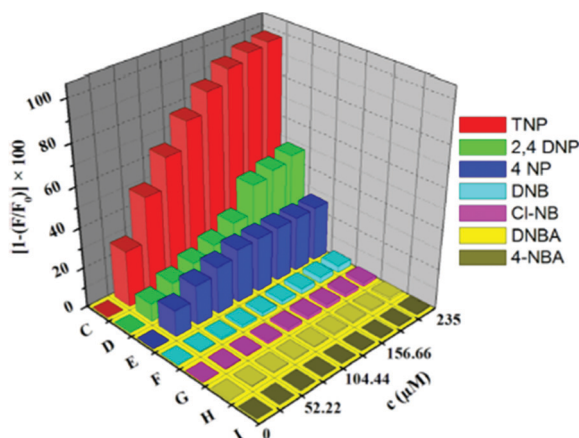
Fig. 24 Quenching efficiency (%) of the excimer fluorescence (at λ_{em} = 467 nm with λ_{ex} = 390 nm) of probe **74** (10 μM) in 8 : 2 H_2O/CH_3CN upon the addition of different NACs. Reprinted from ref. 84, Copyright 2018 American Chemical Society.
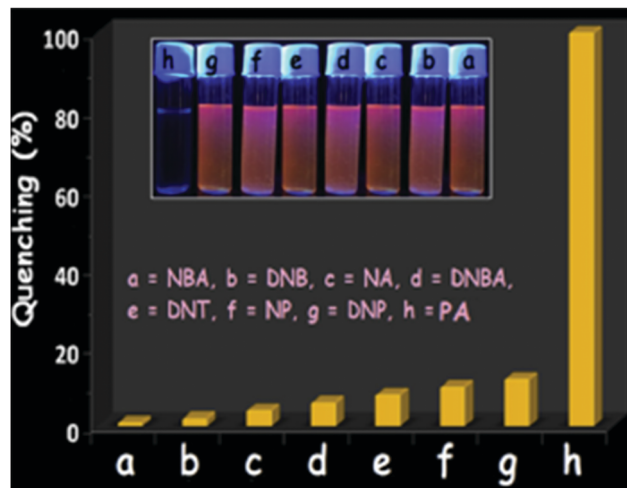
Fig. 25 Quenching efficiency (%) (λ_{em} = 585 nm) of aggregates of **76** with NACs (50 equivalents). Inset: Visual colour change observed with only PA under illumination at 365 nm. Reprinted from ref. 86, Copyright 2019 Elsevier.

limit were calculated to be $2.03 \times 10^4 \, \text{M}^{-1}$ and 0.01 μM, respectively. Probe **75** showed fluorescence quenching by NACs, which followed the order PA > 2,4-DNP > 4-NP > TNB > NM, DNT, NT.

AIE-based probe **76**[86] (Chart 9) showed the formation of J aggregates with an emission maximum at 585 nm in THF–H_2O (1 : 9). These aggregates underwent >98% fluorescence quenching with 4 equivalents of picric acid, with a change in fluorescence colour from orange to dark (Fig. 25), and could detect PA concentrations as low as 0.072 μM in solution. The other NACs caused only a slight change in the fluorescence intensity of **76**. TLC strips coated with aggregates of **76** could detect ∼0.3 pg of PA.

2.5 Protonation of amide-based fluorescent probes for picric acid

Due to the resonance of the nitrogen lone pair with the amide oxygen, the amide oxygen is very electron-rich and easily undergoes protonation. The amide-based probes **77** to **84** exhibit fluorescence quenching upon protonation by picric acid. A comparison of the solvents, LODs, K_{SV} values, emission maxima and applications of probes **77–84** is given in Table 3.

The fluorescent probe **77**[87] (Chart 10) with anthracene and 1,8-naphthalimide units displayed fluorescence enhancement upon the addition of >50% water to its THF solution, which pointed to the formation of aggregates. These aggregates showed ∼88% and ∼30% fluorescence quenching at 508 nm upon the addition of 50 equivalents of picric acid or TNT, respectively. The effect of DNP on the fluorescence of **77** was not evaluated. TD-DFT studies revealed that in the excited state, the intermolecular proton transfer from picric acid to the oxygen of 1,8-naphthalimide is strengthened, which facilitates the non-irradiative PET process to induce the fluorescence quenching.

When the concentration of the tripodal probe **78**[88] was increased to >10 μM in DMSO, a sudden increase in blue fluorescence (λ_{em} = 435 nm) was observed due to the formation
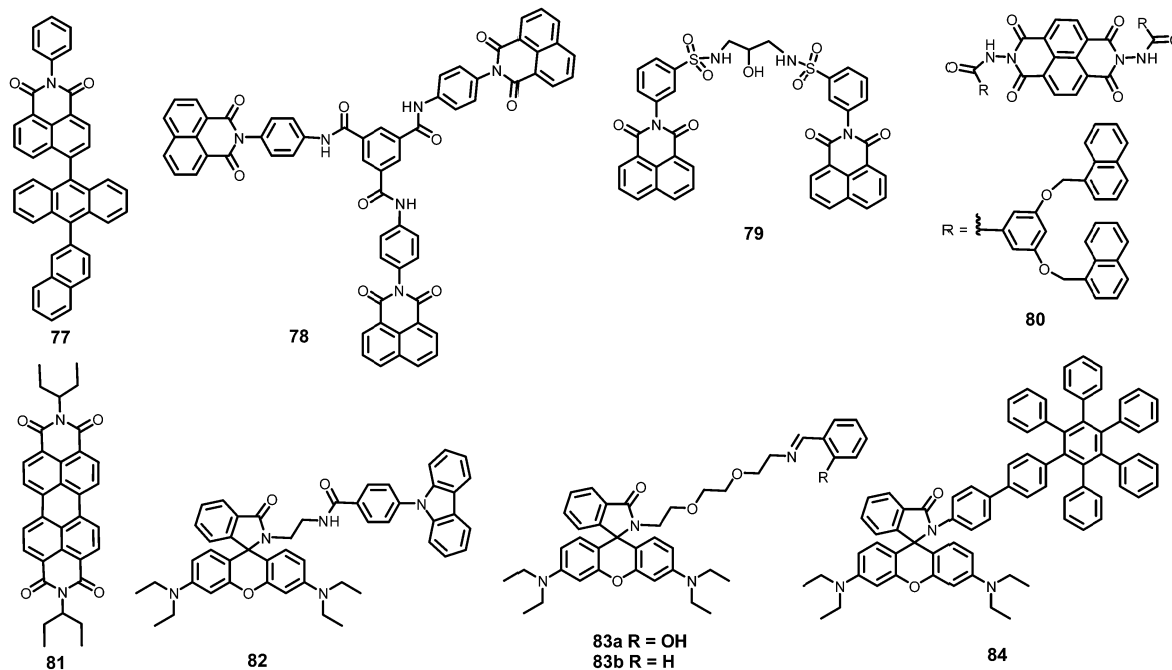
Chart 10 Structures of probes **77–84**.

of self-assembled aggregates. In ^{1}H NMR studies, the down-field shift of the amide NH protons and up-field shift of the aromatic protons with increasing amounts of the probe were highly consistent with the formation of aggregates through π–π and hydrogen bond interactions. These aggregates displayed 99.2% fluorescence quenching with 10 equivalents of picric acid owing to protonation at the amide oxygen, which resulted in the de-aggregation of the molecules of probe **78**. The addition of cyanide ions removed the proton and caused re-aggregation of the molecules of probe **78** to restore the blue emission. Paper strips coated with **78** could detect 10^{-8} M PA.

Probe **79**[89] (Chart 10) showed an AIEE phenomenon at 484 nm in a mixture of DMSO–H$_2$O with increasing amounts of water, and this emission was quenched by 2 equivalents of PA. Picric acid caused much more efficient fluorescence quenching than that observed for 2,4-DNP and 4-NP. Probe **79** formed 1 : 2 (probe **79** : NAC) stoichiometric complexes with picric acid, 2,4-DNP and 4-NP, but the binding constant for picric acid (35×10^7 M^{-1}) was much higher than those for 2,4-DNP (8.71×10^5 M^{-1}) and 4-NP (3.83×10^5 M^{-1}). The partial de-aggregation of the aggregates and π–π interactions with energy transfer from the probe to PA were responsible for the fluorescence quenching. Paper strips coated with probe **79** solution allowed the detection of 10 nM PA by the naked eye (Fig. 26). The paper strips coated with **79** exhibited fluorescence quenching in the presence of PA vapor.

Naphthalene-1,8-diimide derivative **80**[90] (Chart 10) showed excimer emission centred at 600 nm in THF–water (1 : 9) due to the formation of aggregates. The formation of these aggregates was confirmed by SEM and DLS studies. Probe **80** displayed 99% fluorescence quenching at 600 nm with 30 equivalents of
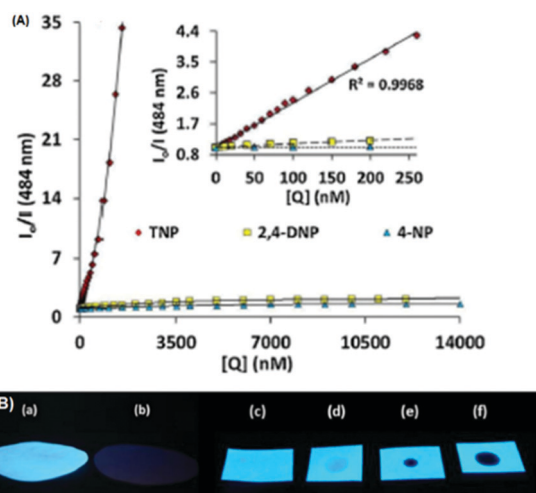
Fig. 26 (A) Fluorescence quenching of probe **79** at 484 nm with PA, DNP, and NP. (B) Fluorescence changes of **79**-coated paper strips (a) before and (b) after being dipped into PA solution (1 μM) or after exposure to (c) H$_2$O or PA solutions with different concentrations: (d) 1 nM, (e) 3 nM, and (f) 10 nM (4 μL), as seen under 365 nm illumination. Reprinted from ref. 89, Copyright 2017 Elsevier.

PA with a fluorescence colour change from orange to dark in THF–water. Probe **80** formed a GSCT complex with PA *via* protonation of the amide oxygen, which was responsible for the fluorescence quenching. The non-phenolic nitroaromatic compounds TNT, ONT, 2,4-DNT and NB induced insignificant changes in the fluorescence of the aggregates. Paper strips coated with probe **80** showed 50% fluorescence quenching with 60 μL of PA solution.
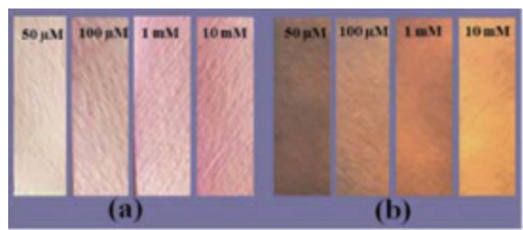
Perylene-based probe **81**[91] (Chart 10) displayed respective 70% and 22% reductions in emission intensity in the presence of picric acid and 2,4-DNP in THF. Non-phenolic NACs caused much smaller fluorescence quenching. Protonation of the amide oxygen of **81** by picric acid and 2,4-DNP formed a non-fluorescent ground state complex. The K_{SV} and detection limit for PA are 6.02×10^3 M^{-1} and 2.98 μM, respectively.

Rhodamine-based fluorescent and colorimetric probe **82**[92] (Chart 10) revealed a new absorption maximum at 560 nm in 5 min with 200 μM PA, with a colour change from colourless to pink and a maximum increase in fluorescence intensity at 586 nm in 80 min due to spiro-lactam ring-opening. The lowest detection limit for PA was found to be 0.82 μM. A Benesi–Hildebrand plot revealed a 1 : 1 stoichiometry between probe **82** and PA with an association constant of 5834 L mol^{-1}. Paper strips coated with probe **82** solution detected 50 μM PA with color change to pink (naked eye) and orange fluorescence under 365 light (Fig. 27).

Rhodamine **83a**[93] (Chart 10) displayed selective detection of PA in MeOH–H$_2$O (1 : 4) with an increase in quantum yield from 0.065 to 0.611. Upon the addition of PA, the appearance of a new absorption maximum at 554 nm and a 99-fold enhancement in emission intensity at 581 nm were observed for probe **83a** due to spirolactam ring opening. Probe **83a** could detect PA concentrations as low as 2×10^{-11} M. Probe **83b** lacking an OH moiety on the Schiff-base was only weakly sensitive to picric acid.

Rhodamine-appended hexaphenylbenzene-based probe **84**[94] (Chart 10) with PA in methanol showed a colour change from colourless to pink (naked eye) and non-fluorescent to red (under 365 nm light). Probe **84** did not exhibit any emission band, but the addition of 30 equivalents of PA resulted in a 147-fold enhancement at 578 nm ($\Phi = 0.82$). Other NACs, such as 4-NP, 2,4-DNP, 2-NT, 2,4-DNT, 1,4-BQ, NM, 1,4-DNB, benzoic acid and 4-NBA did not cause any fluorescence or daylight colour change. The colour/fluorescence change was reversed with tetrabutylammonium hydroxide. Probe **84** could detect PA concentrations as low as 0.035 μM. Proton transfer from picric acid to the spiro-lactam ring resulted in opening of the spiro-lactam ring of rhodamine to the amide and activated the TBET process in **84** *via* the conjugated linker from the donor to the acceptor. TLC strips (Fig. 28) coated with the probe displayed a color change from colourless to pink and could detect 10^{-8} M PA.

3. Positively charged probes for the detection of picric acid

Due to the ease of the dissociation of picric acid to the picrate anion, it can form a neutral electrostatic complex with positively charged fluorophores, thus leading to the proximity of the fluorophore to the picrate anion and efficient electron/energy transfer processes. Positively charged probes bearing dialkylamino moieties can undergo protonation with picric acid and restrict the ICT from the dialkylamino moiety to the rest of the molecule. This restriction of ICT leads to a non-fluorescent complex in the presence of picric acid. These probes have been classified as mono-, di- and tripodal fluorescent derivatives, and are discussed in this order. A comparison of the solvents, LODs, K_{SV} values, emission maxima and applications of probes 85–128 has been presented in Table 4.

3.1 Monopodal cationic fluorescent probes for picric acid

The quinoline derivatives **85** and **86**[95] (Chart 11) having electron-donor groups on the quinoline moiety exhibited emission maxima at 580 nm and 593 nm, respectively, in MeOH–H$_2$O (9 : 1), which revealed 86% and 87% fluorescence quenching with 100 ppm PA, whereas derivative **87**[95] was silent to the presence of PA. In the ^{1}H NMR spectrum of **85**, the lack of change in the chemical shift values even after the addition of 5 equivalents of picric acid suggested no protonation of the fluorophore, and DFT calculations indicated that electron transfer from the LUMO of the fluorophore to the picrate anion was the cause of the fluorescence quenching. In probe **86**, a change in the chemical shifts in its ^{1}H NMR spectrum upon the addition of PA pointed to restriction of ICT and the formation of a non-fluorescent complex. Therefore, probes **85** and **86** followed different mechanisms for fluorescence quenching by picric acid. Thin films of probes **85–87** emitted in the orange-to-red region. Upon exposure to TFA vapor, the fluorescence colour of the film of probe **85** changed from orange to red, and the fluorescence of films of **86** and **87** was completely quenched without any appreciable shift in the emission maxima. These effects were reversed upon interaction with TEA vapor.

The ratiometric probe **88**[96] (Chart 11) in a 100% aqueous medium displayed a red shift in fluorescence maximum from 390 to 440 nm after the addition of PA with a fluorescence colour change from blue to cyan (Fig. 29). The formation of a new emission band at 440 nm was assigned to the protonation of **88** at the quinoline nitrogen. A plot of the I_{455nm}/I_{390nm} ratio with PA concentration showed a good linear relationship between 0.5 μM and 20 μM. This probe was able to detect PA from real samples.
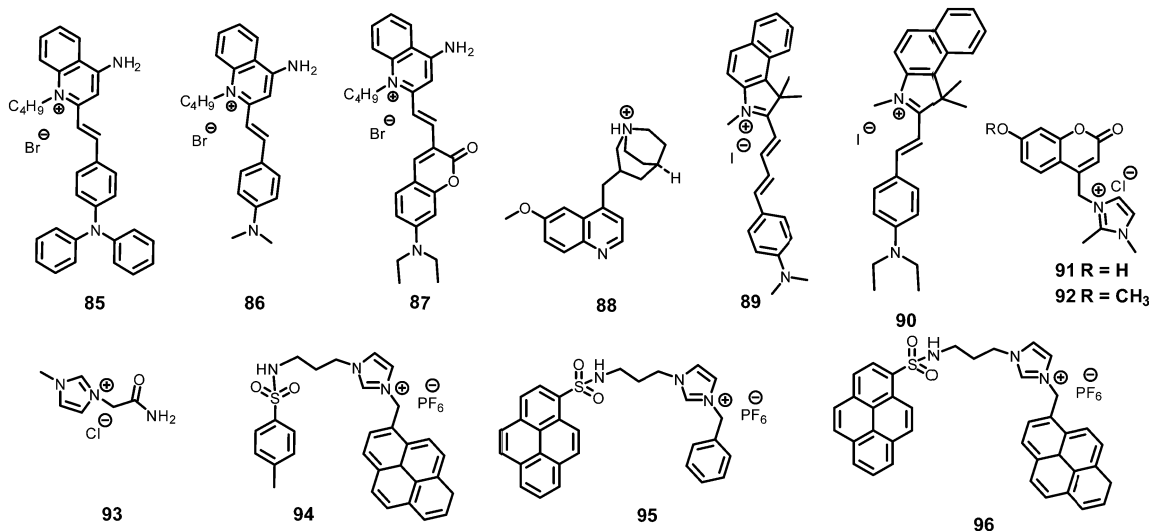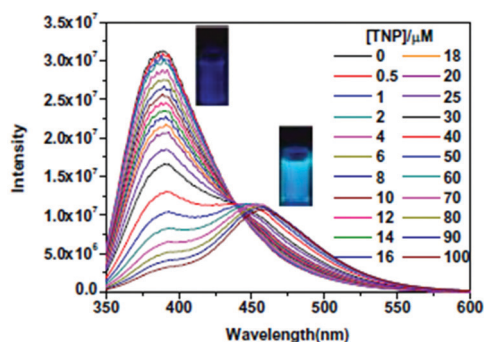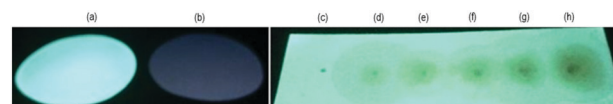
Chart 11 Structures of probes **85–96**.

Fig. 29 Changes in the emission spectrum and emission colour of **88** (1.0 × 10⁻⁵ M) with increasing amounts of PA. Reprinted from ref. 96, Copyright 2019 Elsevier.

Fig. 30 Fluorescence changes of probe-**96**-coated paper strips with PA; (a) a **96**-coated paper strip, (b) a **96**-coated strip dipped in 1 μM PA solution (in 100% water), and a **96**-coated strip upon exposure to 5 μL of aqueous solutions with the following concentrations of PA: (c) 0, (d) 5 nM, (e) 10 nM, (f) 20 nM, (g) 50 nM, and (h) 100 nM. Observed under 365 nm light. Reprinted from ref. 100. Copyright 2016 Elsevier.

Indolium-based probes **89** and **90**[97] (Chart 11) in a THF–H₂O (1:1) mixture exhibited 92% and 93% fluorescence quenching at their maxima of 510 nm and 620 nm for **89** and 720 nm for **90** with the incremental addition of PA solution. The protonation of the *N,N*-dialkylamino moiety by PA restricted ICT and was responsible for the fluorescence quenching. Paper strips coated with **89** and **90** could be used for detecting PA from real samples.

Coumaryl-linked imidazolium salts **91** and **92**[98] (Chart 11) showed decreased fluorescence intensity at 480 nm and 410 nm, respectively, with increasing concentration of PA due to the formation a GSCT complex, as evidenced by ¹H NMR, UV-Vis and fluorescence lifetime studies. Among the other NACs, only 4-NP exhibited a fairly strong interaction with **91** and **92**. These probes were able to detect PA using probe-coated TLC plates. Ionic liquid-based fluorophore **93**[99] (Chart 11) demonstrated 91% and 93% fluorescence quenching with PA and 4-NP, respectively, caused by the formation of a GSCT complex. The information for 2,4-DNP is not available.

Pyrene-appended imidazolium salts **94–96**[100] (Chart 11) could detect PA with little interference from 2,4-DNP and 4-NP

in PBS–DMSO (99.5:0.5) solution. The green emission of probe **96** was completely quenched with PA, and it formed a 1:2 stoichiometric complex. The loss of π–π interactions between the two pyrene rings and electron transfer from pyrene to PA were responsible for the fluorescence quenching. Probes **94** and **95** also showed fluorescence quenching of their monomer emission bands. Paper strips (Fig. 30) coated with **96** were able to detect PA.

Squaraine–dansyl conjugate **97**[101] (Chart 12) displayed a ratiometric change in absorbance and fluorescence upon titration with PA in CH₃CN. With increasing amounts of PA, the solution of **97** exhibited reduced absorbance at 663 nm with the appearance of a new absorption maximum at 627 nm. Upon excitation at 620 nm, probe **97** displayed a blue-shift in fluorescence maximum from 684 nm to 644 nm. The plot of FI₆₄₄ₙₘ/FI₆₈₄ₙₘ with PA shows good linearity in the range 5–100 μM, and the lowest detection limit was 70 nM. In probe **97**, protonation of the dimethylamine nitrogen restricted ICT and the twisted dimethylamino phenyl unit prevented π–π interactions of the squaraine plane with PA, reducing the efficiency of electron and energy transfer. Paper strips coated with probe **97** could detect PA with a color change from a blue to a brownish color (Fig. 31).

3.2 Dipodal dicationic fluorescent probes for picric acid

The fluorescent probe **98**[102] (Chart 12) exhibited a varied distribution in differently charged micelles, which further
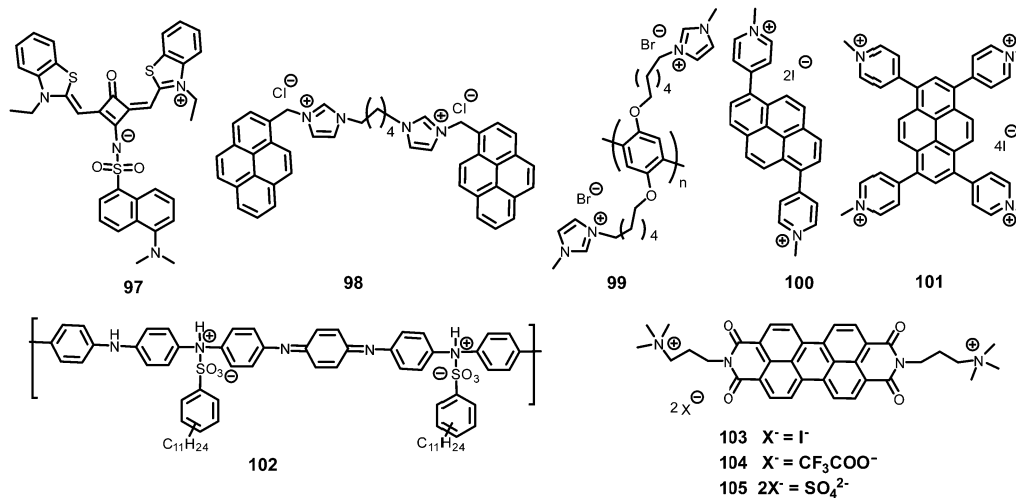
Chart 12 The structures of probes **97**–**105**.

Fig. 31 Visual color changes of probe-**97**-coated paper strips with different amounts of PA; the [PA] values are (A) 10^{-2} M, (B) 10^{-4} M, (C) 10^{-6} M, (D) 10^{-9} M, (E) 10^{-11} M, and (F) no PA. Reprinted from ref. 101, Copyright 2013 Royal Society of Chemistry.
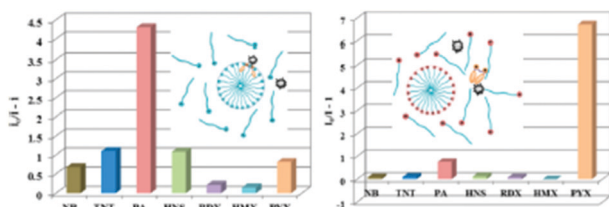

Fig. 32 Fluorescence quenching efficiency of explosives. (left) Probe **98** (1 μM)−SDS (8 mM) sensor system; (right) Probe **98** (1 μM)−DTAB (14 mM) sensor system. [explosives] = 100 μM. Reprinted from ref. 102, Copyright 2014 American Chemical Society.
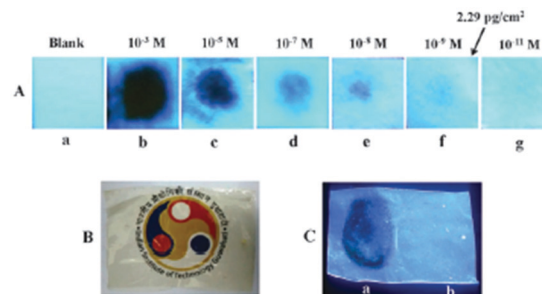

Fig. 33 (A) The colour of fluorescent test strips under UV light (a) before and after (b−g) treatment with 10 μL of solutions of various concentrations of PA. (B) Probe-**99**-doped transparent chitosan film in daylight. (C) Visualization of **99**-doped CS fluorescent film under UV light: (a) dark spot of a residual PA thumbprint and (b) a thumb impression as a control (at 365 nm). Reprinted from ref. 103, Copyright 2015 Royal Society of Chemistry.

influenced the sensing behaviour of the obtained micellar sensor systems towards explosives. The UV-Vis, steady-state and time-resolved emission studies revealed that probe **98** is encapsulated by SDS, but not by the cationic surfactant DTAB. The solution of **98** in SDS showed preferential fluorescence quenching with PA (Fig. 32), but in DTAB solution, the most selective quenching was observed with PYX. The quenching mechanism of the two micellar sensor systems by explosives was static in nature.

Imidazolium-based conjugated polyelectrolyte **99**[103] (Chart 12) revealed fluorescence quenching efficiency following the order PA > 2,4-DNP > 4-NP, but neutral NACs did not cause fluorescence quenching. The ease of the dissociation of PA in water accelerated the electrostatic interaction with cationic probe **99** and resulted in a decrease in emission intensity at 406 nm with a colour change from blue to dark under UV light. Paper strips coated with **99** could detect 2.29 pg cm^{-2} PA. A transparent fluorescent film of commercial chitosan with 5% of probe **99** was also used for the detection of PA (Fig. 33).

Pyrenoviologen cationic derivatives **100** and **101**[104] (Chart 12) possessing high quantum yields of 64% and 95%, respectively, displayed electrostatic interactions with picrate anions in water, and electron transfer between them lead to the fluorescence response. The fluorescence emission spectra of **100** (10 μM) at 513 nm and **101** (10 μM) at 482 nm were completely quenched upon the addition of PA (55 μM).

Dodecylbenzene-sulfonic acid (DBSA)-doped polyaniline **102**[105] (Chart 12) in the solvent NMP underwent fluorescence quenching at 475 nm in the order PA > 1,3-DNB ≈ NB. The results with 2,4-DNP and 4-NP were not discussed. The FE-SEM and AFM images of **102** displayed changes in morphology after the addition of PA (Fig. 34).

Perylene diimide probes **103**–**105**[106] (Chart 12) displayed quenching of their yellow fluorescence upon the addition of PA and 4-nitroaniline (4-NA) with equal ease in DMF and water
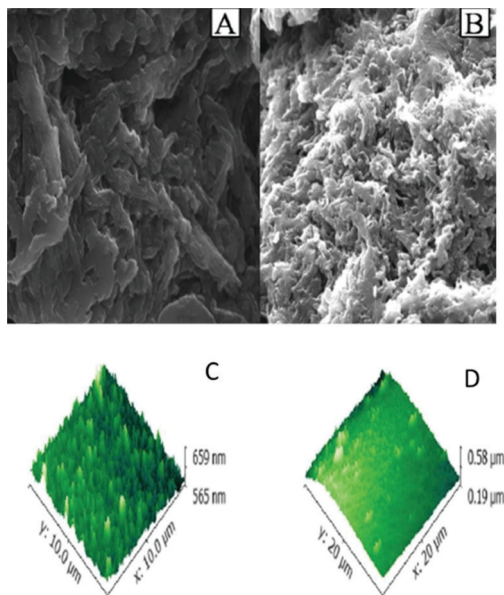
Fig. 34 (a) FESEM images of probe **102** and (b) probe **102** + PA. (c) AFM images of **102** and (d) **102** + PA. Reprinted from ref. 105, Copyright 2018 Wiley Online.

(pH range 1.0 to 10.0). The probes showed stronger fluorescence in DMF than in water.

3.3 Tripodal tricationic fluorescent probes for picric acid

Anthracene-functionalized tris-imidazolium salts **106–107**[107] (Chart 13) found applications for the detection of picric acid in organic and aqueous media. Both **106** and **107** exhibited characteristic anthracene monomer emission in DMSO, with 92% and 91% quenching, respectively, upon the addition of
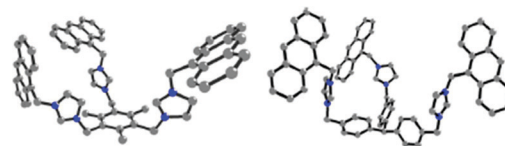
Fig. 35 The X-ray crystal structure of **106** (left) and the energy-optimized structure of **107** (right). Reprinted from ref. 107, Copyright 2013 American Chemical Society.

100 equivalents of PA. Other NACs displayed much smaller fluorescence quenching, but the study with 2,4-DNP – the most interfering nitrophenol – is not available. Probes **106** and **107** showed static quenching due to the ground-state charge-transfer complex formation. X-ray diffraction and computational studies reveal that from among several possibilities, **106** and **107** adopt a *cis,cis,cis* conformation and exhibit a bowl-shaped structure in the solid state (Fig. 35). The ^{1}H NMR and DFT studies of **106** and **107** with PA and the X-ray crystal structure of complex of 106 with PA showed the formation of 1:2 stoichiometric probe ∩ 2PA complex *via* the replacement of two bromide ions with picrate anions.

The X-ray crystal structures and DFT optimization studies of tripodal probes **108** and **109**[108] (Chart 13) show that the three biphenyl substituents are oriented on the same side of the triethylbenzene to form a pseudo-cavity, which is more pre-organised for the encapsulation of PA in comparison to **106** and **107**. Upon excitation at 290 nm, the solution of **108** displayed a decrease in the emission intensity at 402 nm due to a combination of electrostatic, hydrogen-bonding and π–π interactions with the picrate anion (Fig. 36). The Job's plot of **108** revealed a 1:1 stoichiometric complex with PA with a $\log \beta_{11}$ value of 5.82 ± 0.06. The solution of **109** in HEPES buffer displayed a decrease in emission intensity at 470 nm with a colour change
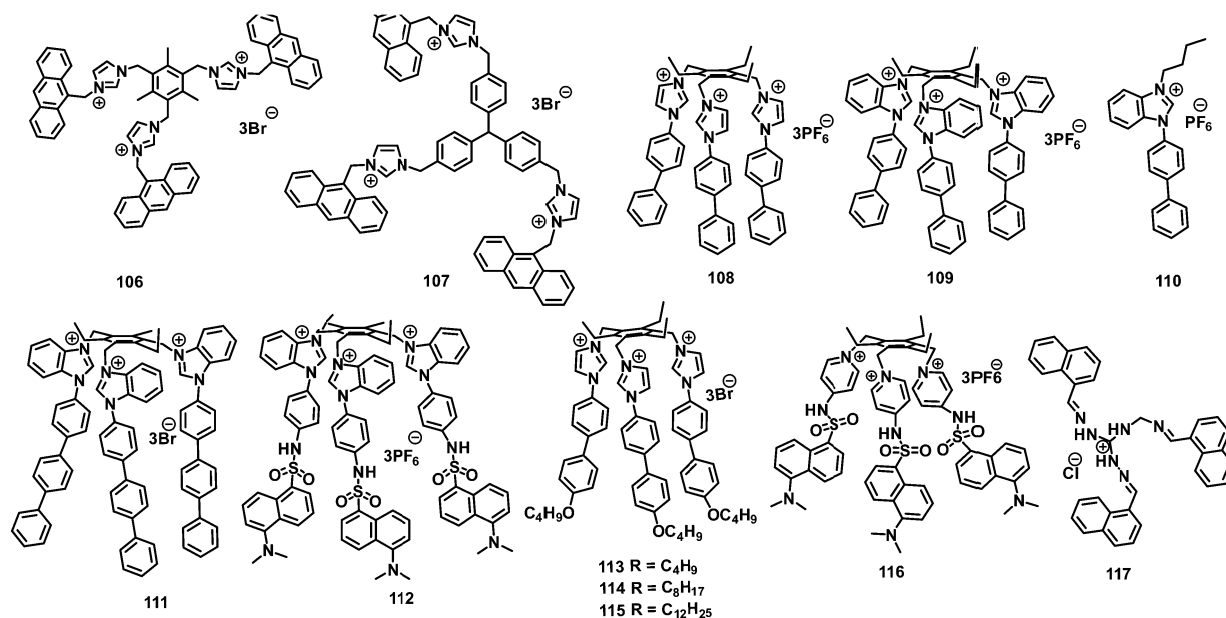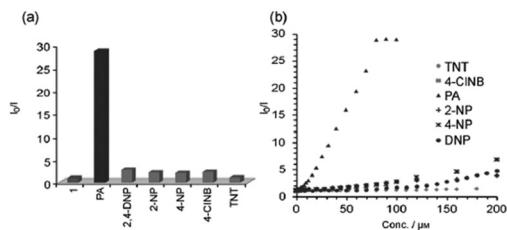

Chart 13 Structures of probes **106–117**.

Fig. 36 (a) Quenching efficiency of **108** with NACs. (b) Stern–Volmer plots of the effects of various NACs on the fluorescence intensity of **108** (HEPES buffer/DMSO (98 : 2)). Reprinted from ref. 108, Copyright 2014 Wiley Online.

from blue to dark in the presence of PA. The poor efficiency of monopod **110** towards PA further highlighted the role of pre-organization in **108** and **109** for the highly sensitive and selective recognition of PA. The significant up-field shift ($\Delta\delta = 0.8$ ppm) of the PA protons in ^{1}H NMR titration studies confirmed that PA was encapsulated in the cavity of **108** and **109**. Paper strips coated with probe **109** detected 137 ag cm^{-2} PA in solution. The paper strips of **109** could also detect PA vapor in 120 s.

Tripod **111**[109] (Chart 13), with an extended hydrophobic pseudo-cavity in comparison to the biphenyl in **108** due to the presence of the triphenylene moiety, could detect 5×10^{-13} M PA in water (2% DMSO) and 2.29×10^{-20} g cm^{-2} PA using coated paper strips. The molecules of **111** self-assembled to form a rod-like morphology in an aqueous medium, as observed through field-emission SEM, TEM and dynamic light scattering studies. With the gradual addition of PA, these aggregates underwent an aggregation–disaggregation process to form complex morphological structures (10^{-12}–10^{-10} M PA) and then spherical aggregates at 10^{-9}–10^{-8} M PA (Fig. 37). Further increasing the amount of PA to 10^{-7}–10^{-6} M resulted in the dissolution of these spherical aggregates to give well-dispersed spheres. During fluorescence studies, these aggregates demonstrated super-amplified fluorescence quenching ($>97\%$) by 10^{-5} to 0.2 equivalents of PA. Thin films of tripod **111** exhibited fluorescence quenching within 6 min in the presence of PA.

Dansyl-conjugated probe **112**[110] (Chart 13) in HEPES buffer (2% DMSO) showed amplified quenching at 540 nm in the
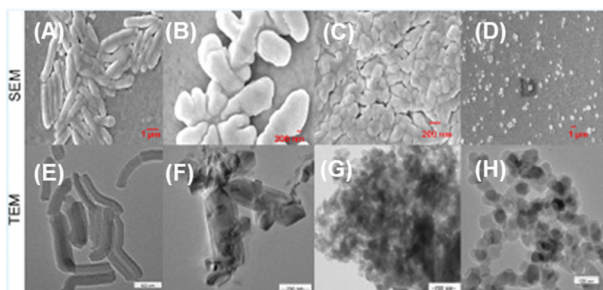

Fig. 37 Morphological (upper panels: SEM images, lower panels: TEM images) changes in TRIPOD **111** upon the addition of various amounts of picric acid: (A and E) [PA] = 0 M, (B, F) [PA] = 10^{-12} M, (C, G) [PA] = 10^{-8} M, and (D, H) [PA] = 10^{-7} M. Reprinted from ref. 109, Copyright 2015 American Chemical Society.
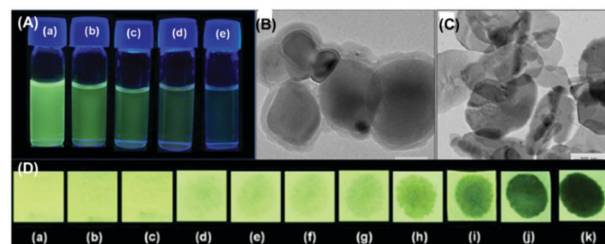

Fig. 38 (A) Visual fluorescence changes of probe **112** in blank solution (a) and with increasing concentrations of PA: (b) 50 pM, (c) 1 nM, (d) 2 nM, and (e) 4 nM. (B and C) TEM images of (B) probe **111** (1 μM) and (C) probe **111** (1 μM) + PA (10 μM). (D) Photographs of probe-**112**-coated paper strips (under 365 nm UV light): (a) a virgin test strip, (b) a paper strip with a drop of water, and strips with 6 μl of PA solutions with concentrations of (c) 10^{-14} M, (d) 10^{-13} M, (e) 10^{-12} M, (f) 10^{-11} M, (g) 10^{-10} M, and (h) 10^{-9} M. Reprinted from ref. 110, Copyright 2016 Elsevier.

presence of PA, with an associated change in the fluorescence color from yellow to dark (Fig. 38A). The morphology of probe **112** (Fig. 38B) changed after the addition of 1 equivalent of PA (Fig. 38C). Paper strips coated with **112** detected 13.7 ag cm^{-2} PA using the contact mode method (Fig. 38D). Probe **112** exhibited a combination of electrostatic and hydrophobic π–π interactions with the picrate anion.

Imidazolium-based fluorescent probes **113–115**[111] (Chart 13) were used for the detection of nitroaromatics such as PA, 2,4-DNP, TNT and ClDNB in water–DMSO (98 : 2). Among the three probes, probe **113** did not undergo aggregation and remained in the molecularly dissolved state due to its short alkyl chains, but the other two probes (**114** and **115**) self-assembled in water.

Upon excitation at 290 nm, probes **113–115** displayed emission maxima at 454 nm, 448 nm and 412 nm, respectively. Upon the addition of 0.1 equivalents of nitroaromatic derivatives such as PA, 2,4-DNP, TNT and Cl-DNB to a solution of **114**, 92%, 89%, 73% and 51% quenching of the emission intensity was observed, respectively. Similarly, probe **115** also showed 94%, 93%, 73% and 66% fluorescence quenching with PA, 2,4-DNP, TNT and Cl-DNB, respectively. Probe **114** is 10, 6000, and 16 000 times more selective towards PA in comparison to 2,4-DNP, TNT and Cl-DNB due to the RET process. Paper strips coated with probe **114** detected 2.29×10^{-20} g cm^{-2} PA (Fig. 39A–Q) by the contact mode, whereas probes **113** and **115** were less sensitive to PA. Probe **114** showed morphological changes after the addition of PA (Fig. 39b–e). Probes **114** and **115** could detect PA in the vapor phase in 30 s.

Pyridinium–dansyl conjugate-based tripod **116**[112] (Chart 13) underwent aggregation in water (2% DMSO) with emission at 480 nm ($\Phi = 0.71$), and these aggregates displayed amplified fluorescence quenching with only PA owing to the excited state energy transfer from **116** to PA. Other NACs, including the nitrophenols 2,4-DNP and 4-NP, had minimal effect on the fluorescence of the aggregates of **116**. Probe **116** exhibited a linear change in fluorescence over a large range of PA concentration from 10^{-13} to 10^{-5} M. SEM and TEM images revealed changes in the morphology of probe **116** from leaf-like structures to a spherical shape with PA (Fig. 40a–f). Paper strips coated with
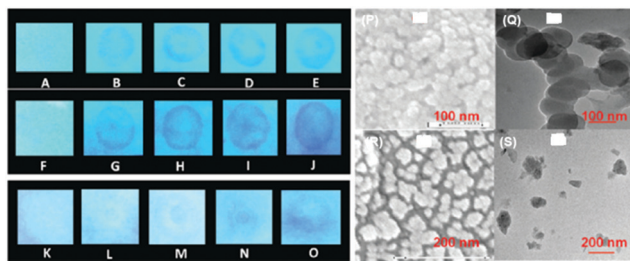
Fig. 39 Fluorescence of probe-coated paper strips upon interaction with 10 μl of solutions with different concentrations of PA. (A–E) Probe **113** with (A) water; (B) 10^{-13} M PA; (C) 10^{-11} M PA; (D) 10^{-9} M PA; and (E) 10^{-7} M PA. (F–J) Probe **114** with (F) water; (G) 10^{-17} M PA; (H) 10^{-15} M PA; (I) 10^{-13} M PA; and (J) 10^{-11} M PA. (K–O) Probe **115** with (K) water; (L) 10^{-17} M PA; (M) 10^{-15} M PA; (N) 10^{-13} M PA; and (O) 10^{-11} M PA. SEM (P) and TEM (Q) images of probe **114** alone, and (R) and (S) probe **114** with PA (1 equiv.). Reprinted from ref. 111, Copyright 2016 Royal Society of Chemistry.

probe **116** could detect 137 fg cm^{-2} PA in the solid state (Fig. 40g). The fluorescence lifetime of **116** increased from 0.73 ns to 1.45 ns in the presence of PA, which pointed to dynamic fluorescence quenching of aggregates of **116** with sub-micromolar amounts of PA.

The tripodal Schiff base **117**[113] (Chart 13) with H-bonding donor triaminoguanidinium moieties, the requisite hydrophobicity and π-electron-rich naphthalene moieties formed π-stacked crystals. When dispersed in water, these crystals[113] displayed fluorescence quenching at 480 nm in accordance with the acidity of the phenolic

protons in the order PA > 2,4-DNP > 4-NP, but neutral NACs caused minimal fluorescence quenching.

The stilbazolium-based dipodal[114] probe **118** (Chart 14) with both absorption and emission in the visible region formed aggregates with an absorption maximum at 475 nm (red colour), which demonstrated a highly selective and sensitive change in colour from red to light-yellow with picric acid. The LOD for picric acid is 100 pM, which is the lowest in the literature using UV-Visible spectroscopy. These aggregates with fluorescence in the red region (615 nm) exhibited fluorescence quenching selectively with picric acid. TNT and other NACs induced inconsequential changes in the visible spectrum of the aggregates of **118**, even when present in excess.

Upon the addition of water to its DMSO solution, tripod **119**[115] (Chart 14) displayed aggregation-based fluorescence
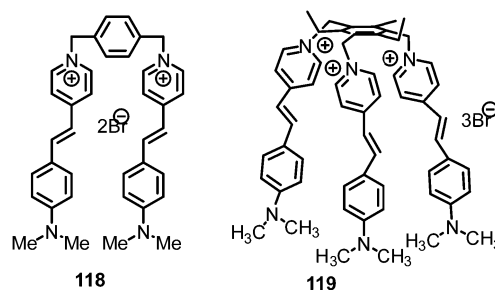

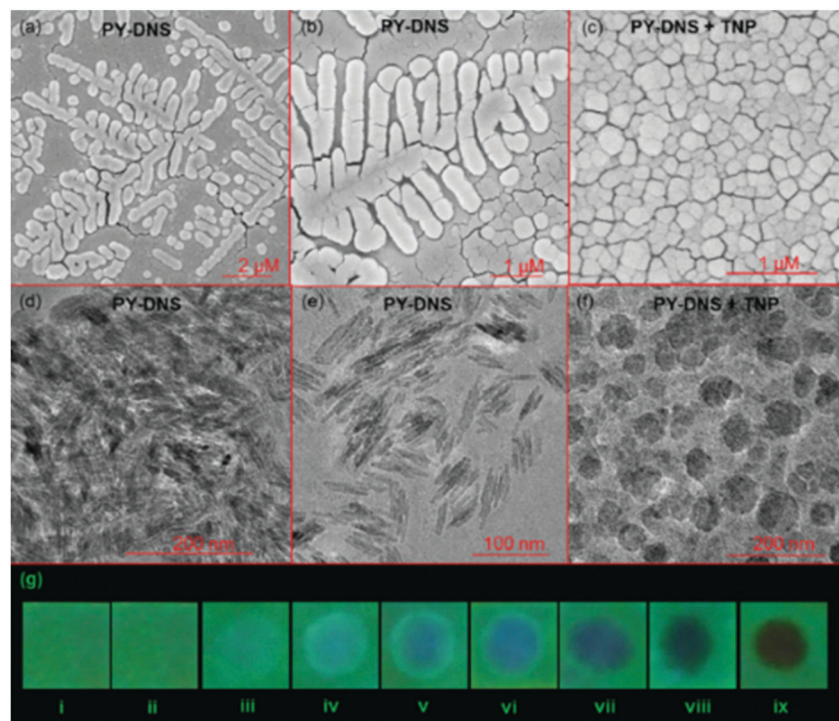**Chart 14** Structures of probes **118** and **119**.

Fig. 40 (a and b) SEM images of thin films of **116** alone and (c) a **116** and PA (1 : 1) solution obtained on a glass plate. (d and e) TEM images of two different sections of thin film of **116**. (f) A TEM image of thin film from the 1 : 1 solution of **116** and PA. (g) Photographs of probe **116**-coated paper strips: (i) a virgin test strip; (ii) a strip with water; (iii–ix) strips with 6 μL of solutions of PA with different concentrations: (iii) 10^{-13} M; (iv) 10^{-12} M; (v) 10^{-11} M; (vi) 10^{-10} M; (vii) 10^{-9} M; (viii) 10^{-8} M; and (ix) 10^{-7} M. Reprinted from ref. 112, Copyright 2017 Royal Society of Chemistry.
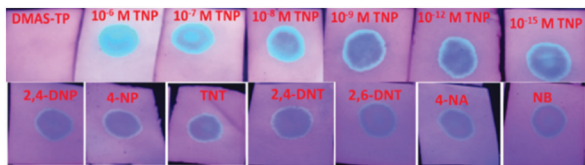
Fig. 41 Paper strips coated with probe **119** (DMAS-TP) (1 mM) demonstrated changes in their fluorescence upon treatment with solutions of varying concentrations of picric acid and 10^{-6} M solutions of other NACs (10 µl each). Reprinted from ref. 115, Copyright 2021 Royal Society of Chemistry.

quenching with a blue-shift in emission maximum from 635 nm to 615 nm, pointing to the formation of H-aggregates. These aggregates with picric acid exhibited simultaneous fluorescence reduction at 615 nm and an increase in fluorescence intensity between 510–540 nm, leading to ratiometric behaviour for picric acid. Paper strips coated with aggregates of **119** differentiated PA from other NACs through a fluorescence colour change from pink-red to blue with picric acid only (Fig. 41) and provided unprecedented discrimination of TNP from other NACs. Silica nanoparticles with probe 119 adsorbed on them highlighted latent fingerprints on a variety of substrates including aluminium foil, metal sheets, coins, ceramic tiles, *etc.*, with a high resolution with possible applications in modern forensics.

TD-DFT studies of **118** and **119** demonstrated that restriction in ICT owing to proton transfer from picric acid to the dimethylamino group was responsible for the depletion of the colour of the probes with picric acid and that the proximity of the picrate anion to the probe resulted in charge transfer from the picrate to the DMAS moiety, leading to the non-emissive/poorly emissive excited state.

4. Metal complexes for the detection of picric acid

The weak fluorescence of the hydrazone-based probe **120**[116] (Chart 15) in a 95% aqueous medium (5% DMSO) was enhanced with a blue-shift of the emission maximum from 529 nm to 485 nm upon the addition of Al^{3+} ions. The increased fluorescence was assigned to the formation of a stable chelated system with high rigidity. The high fluorescence of the *in situ* prepared **120**–Al(III) ensemble was quenched by the addition of PA, with a detection limit of 12.15 nM. An INHIBIT logic gate was also elaborated using this probe. Furthermore, test strips of **120** were also able to detect the presence of PA. Similarly, another AIEE-active Al(III) complex, **121**,[117] was used for the detection of picric acid in a pure aqueous system and a detection limit of 1.67 µM was calculated. However, the **121**–Al^{3+} ensemble exhibited slightly more quenching with DNP as compared to PA.

The AIEE-based hexaphenylbenzene derivative **122**[118] (Chart 15) exhibited an increase in quantum yield from 0.48 to 0.72 and a 7.14-fold enhancement in emission intensity at 460 nm with 30 equivalents of Hg^{2+} in H_2O–THF (4:6). The 1:1 stoichiometric **122**–Hg^{2+} ensemble was further used for the detection of PA through the fluorescence quenching process. The quenching in FL by PA was assigned to electrostatic interaction between the host and guest and electron transfer from the excited **122**–Hg^{2+} complex to PA, as confirmed by pH and ^{1}H NMR titration studies. Other nitro derivatives, such as TNT, 2,4-DNT, 1,3-DNB, *etc.*, did not show any effect on the fluorescence intensity of this ensemble because of the lack of tendency to protonate the *N,N*-dimethylamino group. Furthermore, paper strips (Fig. 42) coated with **122**–Hg^{2+} could detect PA concentrations as low as 0.03 µM.
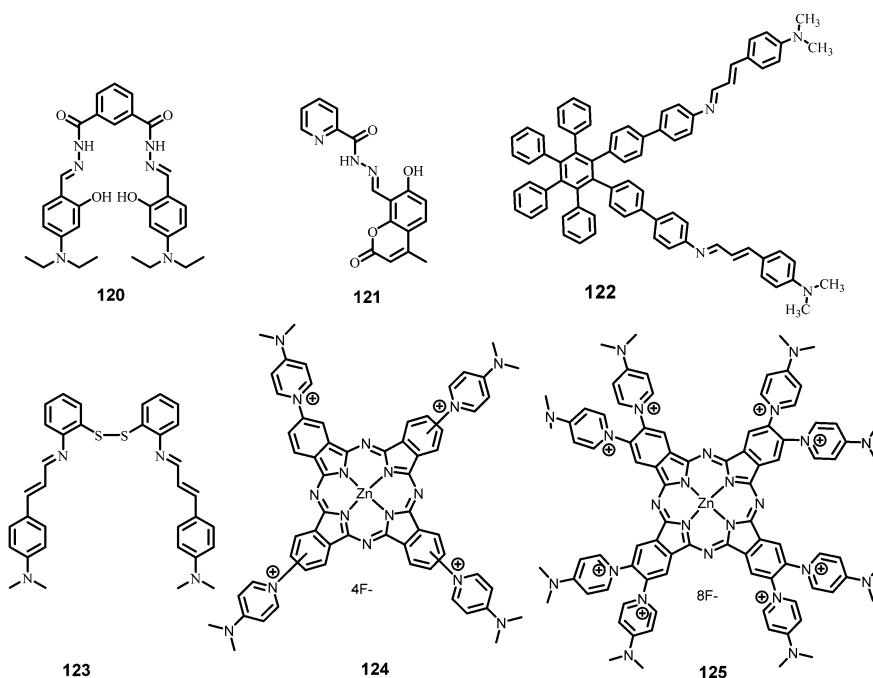

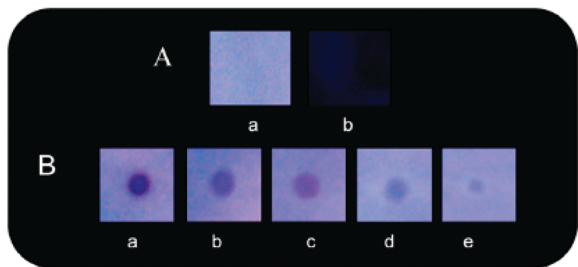**Chart 15** Structures of probes **120–125**.

Fig. 42 (A) Paper strips of the **122**−Hg^{2+} ensemble (a) before and (b) after being dipped into PA solution (10^{-3} M in THF). (B) Demonstration of the effect of different concentrations of PA on test strips of the **122**−Hg^{2+} ensemble [(a) 229 × 10^3 ppm, (b) 229 ppm, (c) 2.29 ppm, (d) 22.9 ppb, and (e) 0.22 ppb]. All images were taken under 365 nm UV illumination. Reprinted from ref. 118, Copyright 2013 American Chemical Society.

Hg^{2+} interacts with the sulphur and the imino nitrogen of probe **123**[119] (Chart 15) to form a 1 : 2 stoichiometric complex **123** ∩ (Hg^{2+})$_2$ with a nearly 290-fold increase in quantum yield from 0.001 to 0.290. The formation of nanoaggregates of **123** ∩ (Hg^{2+})$_2$ was confirmed by the appearance of level-off long wavelength tails in its absorbance spectra. This highly blue-fluorescent **123** ∩ (Hg^{2+})$_2$ complex (λ_{em} = 458 nm) became weakly fluorescent (λ_{em} = 00 nm) with PA, whereas other nitroaromatics such as TNT, 2,4-DNT, 1,3-DNB, nitromethane, NT, NB, and DMDNB did not show any effect on the fluorescence intensity. The protonation of the amine nitrogen followed by electron transfer from **123** (Hg^{2+})$_2$ to PA was responsible for the fluorescence quenching mechanism. NOR and INHIBIT logic gates were also constructed using PA and H$^+$ as inputs, and emission at 458 and 404 nm as outputs.

The water-soluble ZnPc derivatives **124** and **125**[120] (Chart 15) with four and eight 4-dimethylaminopyridines gave quantum yields of 0.11 and 0.16, respectively, in DMSO. Probes **124** and **125** showed 87% and 89% fluorescence quenching at 680 nm and 695 nm, respectively, with 10 equivalents of PA due to the protonation of the *N*,*N*-dimethyl amino units, which prevented intramolecular charge transfer from the dimethylamino groups to the macrocycle core. Both probe **124** and **125** followed the quenching order NM < NB < NT < 4-NP < 2,4-DNT < 2,4-DNP < TNT < PA and could detect PA concentrations as low as 0.7 ± 0.1 and 1.1 ± 0.1 ppm, respectively. The thin films of **124** and **125** showed 28.6, 9.8, 9.2, and 7.5% fluorescence quenching in 240 s by the vapor of PA, TNT, 2,4-DNP, and 2,4-DNT, respectively.

5. Miscellaneous

BODIPY derivative **126**[121] (Chart 16) displayed 95% quenching of the emission intensity at 600 nm in the presence of 500 equivalents of PA due to the enhancement in intermolecular PET. The down-field shift of the ^{19}F NMR signal in the presence of PA supported hydrogen bonding between fluorine and the phenolic hydrogen of PA. All other NACs resulted in less than 30% fluorescence quenching. Furthermore, **126** can be used for instant visualization of traces of PA.
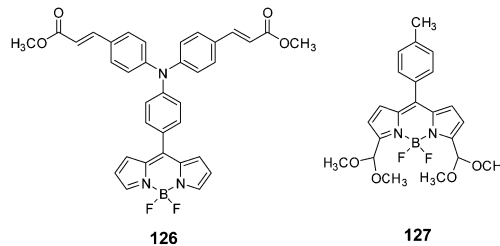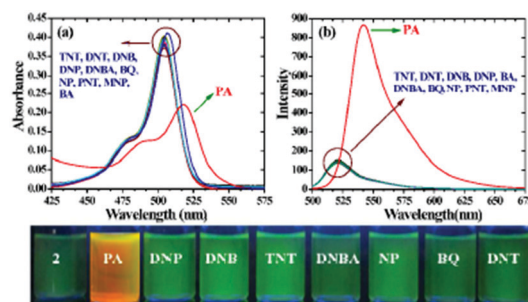

Chart 16 Structures of probes **126** and **127**.

Fig. 43 Changes in the (a) absorption and (b) emission intensity of BODIPY **126** (5 μM) with nitroaromatics (50 equiv.) in CH$_3$CN–H$_2$O (9 : 1; v/v) solution. Bottom panel: Color changes observed upon the addition of various nitroaromatic compounds to BODIPY **126** under a UV lamp. Reprinted from ref. 121, Copyright 2015 Royal Society of Chemistry.

BODIPY-based turn-on chemodosimeter **127**[122] (Chart 16) exploited the strong acidic character of picric acid for highly selective hydrolysis of the acetal to the aldehyde in CH$_3$CN–water (9 : 1). Upon the addition of > 20 equivalents of picric acid, the absorption maximum was red-shifted from 504 to 516 nm and the emission maxima from 518 to 535 nm, along with a six-fold enhancement in the emission intensity (Fig. 43). The fluorescence colour of the solution changed from pale green to bright yellow-orange due to the inhibition of PET. In the solid state, thin films of **127** displayed a red-shifted emission band at 612 nm, which exhibited 83% quenching of its fluorescence intensity upon exposure to saturated PA vapour for 500 s. Other NACs did not cause fluorescence quenching in these films.

BSA protein probe **128**[123] in an aqueous medium displayed 80.1% fluorescence quenching at 348 nm with 20 μM PA due to electron transfer and Förster resonance energy transfer mechanisms, as well as acid–base pairing interactions between the amino groups of **128** and PA. The response and equilibrium time was found to be less than 1 min. The α-helix content of BSA decreased with the addition of PA.

6. Conclusions

Picric acid (pK_a 0.42), one of the most acidic nitroaromatic explosive materials, has the advantage of being able to selectively protonate basic sites such as amines (both aromatic and aliphatic), imines, aza-heterocycles (pyridine, imidazole), amides, *etc.*, that are present in fluorophores. Other closely related nitrophenol

derivatives, such as 2,4-DNP (pK_a 4.04) and 4-nitrophenol (pK_a 7.07), have poor capacity to protonate aromatic amines and other basic sites in comparison to picric acid. The protonation of basic nitrogen/oxygen in the fluorophore activates electrostatic interactions between the protonated fluorophore and the picrate anion. Alternately, the picrate anion can undergo electrostatic interactions with positively charged fluorescent probes. The proximity between the fluorophore and picrate anion that arises due to the strong electrostatic interactions facilitates electron/energy transfer processes and thus leads to selective fluorescence quenching with picric acid over other phenolic and non-phenolic nitroaromatic derivatives. This has defined a distinct feature for the design of fluorescent probes for the selective detection of picric acid over other nitroaromatic compounds.

In general, picric acid is a natural fluorescence quencher *via* either the formation of non-fluorescent ground state charge transfer complexes due to the protonation of the basic site in the fluorophore or due to electron/energy transfer from the fluorophore in the excited state to the ground state of picric acid. However, fluorescence quenching is inherently a negative signal. Molecular probes that show an increase in fluorescence or a shift in the wavelength of the fluorescence maximum upon interaction with an analyte are always preferred, as these provide a positive signal for analysis.

However, FE and ratiometric fluorescence changes in response to PA have only been observed in a limited number of examples. Probe **97**,[101] which is a conjugate of two fluorophores, namely, squaraine and dansyl moieties, displayed a blue-shift in its fluorescence maximum from 684 nm to 644 nm in CH_3CN and CH_3CN–water (9:1). In this case, the protonation of the dimethyl-lamine nitrogen inhibited PET from the dansyl moiety and released the fluorescence of the squaraine moiety. In another case, the BODIPY probe **25**[52] displayed a 300-fold enhancement in emission intensity with PA in ethanol. Another ICT-based probe, **119**,[115] showed the distinct appearance of blue fluorescence upon the treatment of probe-coated paper strips with picric acid. In all these examples, the picric-acid-mediated protonation at the amine nitrogen is the key mechanistic feature. In the curcumin-based probes **27** and **28**,[54] the protonation of the amine by picric acid induced the aggregation of the resulting salts, and thus aggregation-induced emission enhancement was observed.

Furthermore, the detection of picric acid vapor using fluorescent probes can provide an advantage for device formation. However, only a few cases in which thin films[108,109,111,120] of a probe exhibit fluorescence quenching with picric acid within a few minutes have been reported, along with other cases in which a probe deposited on a TLC plate[53,89] or THF–water[33] solutions of a probe detect picric acid vapor.

In future, we anticipate the development of fluorescent probes for picric acid with two or more fluorescent moieties whose signals before and after interaction with picric acid differ, thus providing an increase or ratiometric change in the fluorescence. Fluorescence probes with increased ICT upon protonation with picric acid will appear in the literature, which are expected to display a shift in the fluorescence maximum to longer wave-lengths with or without ratiometric changes. Fluorescence probes

exhibiting a decrease in ICT upon protonation with a blue-shift in the fluorescence maximum will be developed.

Most of the fluorescent probes applied for the detection of picric acid emit in the blue or green region of the visible light spectrum and are plagued by interference from the background fluorescence of natural samples. There are only a few examples of red-emitting probes that have found application in the detection of picric acid. Increasing emphasis will be placed on the development of red- or NIR-emitting probes in future. Such probes are expected to open up new vistas for investigating the effects of PA in live cells and tissues. The development of fluorescent probes for the selective detection of PA vapor is another noteworthy area for future research.

Abbreviations

ACN	Acetonitrile
ACQ	Aggregation-caused quenching
AFM	Atomic force microscopy
AIE	Aggregation-induced enhancement
AIEE	Aggregation-induced emission enhancement
BODIPY	Boron-dipyrromethene
BQ	1,4-Benzoquinone
ClDNB	Chlorodinitrobenzene
CT	Charge transfer
DBSA	Dodecylbenzene-sulfonic acid
DFT	Density functional theory
DLS	Dynamic light scattering
DMF	N,N-Dimethylformamide
DMNB	Dimethylnitrobenzene
DMSO	Dimethyl sulfoxide
DNB	Dinitrobenzene
DNBA	1,4-Dinitrobenzoic acid
2,4- DNP	2,4-Dinitrophenol
2,4-DNT	2,4-Dinitrotoulene
DTAB	Dodecyltrimethylammonium bromide.
ESIPT	Excited-state intramolecular proton transfer
FE	Fluorescence enhancement
FI	Fluorescence intensity
FRET	Förster resonance energy transfer
FQ	Fluorescence quenching
GSCT	Ground-state charge transfer
HCHO	Formaldehyde
HEPES	4-(2-Hydroxyethyl)-1-piperazineethanesulfonic acid
HOMO	Highest occupied molecular orbital
ICT	Internal charge transfer
IFE	Inner filter effect
LOD	Limit of detection
LUMO	Lowest unoccupied molecular orbital
MeOH	Methanol
MOF	Metal organic framework
NA	Nitroaniline
NACs	Nitroaromatics
NB	Nitrobenzene
NM	Nitromethane

NMR	Nuclear magnetic resonance
NMP	N-Methyl-2-pyrrolidone
4-NP	4-Nitrophenol
NT	Nitrotoulene
PA	Picric acid
PBS	Phosphate buffer saline
PET	Photo-induced energy transfer
pK_a	Acid dissociation constant
PYX	2,6-Bis(picrylamino)-3,5-dinitropyridine
RDX	Hexahydro-1,3,5-trinitro-1,3,5-triazine
RET	Resonance energy transfer
RIR	Restricted intramolecular rotation
SDS	Sodium dodecylsulfate
SEM	Scanning electron microscopy
TBET	Through-bond energy transfer
TEA	Triethylamine
TEM	Transmission electron microscopy
TFA	Trifluoroacetic acid
THF	Tetrahydrofuran
TNP	Trinitrophenol
TNT	Trinitrotoulene
TPE	Tetraphenylethylene
V.P.	Vapour pressure

Author contributions

Sukhvinder Dhiman, Nancy Singla, Manzoor Ahmad and Prabhpreet Singh: review writing; Subodh Kumar: conceptualization, review writing and fund raising.

Conflicts of interest

There are no conflicts to declare.

Acknowledgements

References

1 J. Akhavan, *The chemistry of explosives*, Royal Society of Chemistry, 2011.

2 S. Shanmugaraju and P. S. Mukherjee, *Chem. Commun.*, 2015, **51**, 16014–16032.

3 P. Wexler, *Encyclopedia of Toxicology*, 2nd edn, 2005.

4 P. Wexler, *Encyclopedia of Toxicology*, 3rd edn, 2014.

5 M. Russel, *The Chemistry of Fireworks: Edition 2*, 2009, p. 138.

6 P. G. Thorne and T. F. Jenkins, *Special Report*, USA Cold Regions Research and Engineering Laboratory, Hanover, NH, 1995, pp. 95–120.

7 P. G. Thorne and T. F. Jenkins, *Field Anal. Chem. Technol.*, 1997, **1**, 165–170.

8 S. H. Yalkowsky, Y. He and P. Jain, *Handbook of Aqueous Solubility Data*, 2nd edn, CRC Press, Boca Raton, FL, 2010, p. 200.

9 R. M. Hebert and A. M. Jackovitz, *Wildlife Toxicity Assessment for Picric Acid (2,4,6-Trinitrophenol)*, 2015, pp. 271–277.

10 M. Takahashi, H. Ogata, H. Izumi, K. Yamashita, M. Takechi, M. Hirata-Koizumi, E. Kamata, R. Hasegawa and M. Ema, *Congenit. Anom.*, 2004, **44**, 204–214.

11 J. F. Wyman, M. P. Serve, D. W. Hobson, L. H. Lee and D. E. Uddin, *J. Toxicol. Environ. Health*, 1992, **37**, 313–327.

12 (a) K. R. Cooper, D. T. Burton, W. L. Goodfellow and D. H. Rosenblatt, *J. Toxicol. Environ. Health*, 1984, **14**, 731–747; (b) K.-M. Wollin and H. H. Dieter, *Arch. Environ. Contam. Toxicol.*, 2005, **49**, 18–26.

13 J. Y. Shen, J. F. Zhang, Y. Zuo, L. J. Wang, X. Y. Sun, J. S. Li, W. Q. Han and R. He, *J. Hazard. Mater.*, 2009, **163**, 1199–1206.

14 (a) M. E. Germain and M. J. Knapp, *Chem. Soc. Rev.*, 2009, **38**, 2543–2555; (b) Y. Salinas, R. Martınez-Manez, M. D. Marcos, F. Sancenon, A. M. Costero, M. Parraad and S. Gilad, *Chem. Soc. Rev.*, 2012, **41**, 1261–1296; (c) G. V. Zyryanov, D. S. Kopchuk, I. S. Kovalev, E. V. Nosova, V. L. Rusinov and O. N. Chupakhin, *Russ. Chem. Rev.*, 2014, **83**, 783–819.

15 (a) K. K. Kartha, A. Sandeep, V. K. Praveen and A. Ajayaghosh, *Chem. Rec.*, 2015, **15**, 252–265; (b) X. Sun, Y. Wang and Y. Lei, *Chem. Soc. Rev.*, 2015, **44**, 8019–8061; (c) S. Shanmugaraju and P. S. Mukherjee, *Chem. – Eur. J.*, 2015, **21**, 6656–6666; (d) M. Chhatwal, R. Mittal, R. D. Gupta and S. K. Awasthi, *J. Mater. Chem. C*, 2018, **6**, 12142–12158; (e) E. V. Verbitskiy, G. L. Rusinov, O. N. Chupakhin and V. N. Charushin, *Dyes Pigm.*, 2020, **180**, 108414; (f) A. S. Tanwar, N. Meher, L. R. Adil and P. K. Iyer, *Analyst*, 2020, **145**, 4753–4767.

16 M. E. Walsh, *Talanta*, 2001, **54**, 427–438.

17 P. T. Sukhanov, A. A. Kushnir, E. V. Churilina, N. V. Maslova and G. V. Shatalov, *Anal. Chem.*, 2017, **72**, 468–472.

18 (a) J. Yinon, *Mass Spectrom. Rev.*, 1982, **1**, 257–307; (b) J. C. Mathurin, T. Faye, A. Brunot and J. C. Tabet, *Anal. Chem.*, 2000, **72**, 5055–5062; (c) A. Prakash, S. Chandra and D. Bahadur, *Carbon*, 2012, **50**, 4209–4219; (d) D. Lin, J. Wu, M. Wang, F. Yan and H. Ju, *Anal. Chem.*, 2012, **84**, 3662–3668.

19 (a) M. Krausa and K. Schorb, *J. Electroanal. Chem.*, 1999, **461**, 10–13; (b) C. L. M. Palenzuela, F. Novotný, P. Krupička, Z. Sofer and M. Pumera, *Anal. Chem.*, 2018, **90**, 5753–5757; (c) A. Ramachandran, J. S. Arya Nair and S. K. Yesodha, *ACS Sustainable Chem. Eng.*, 2019, **7**, 6732–6743.

20 (a) J. M. Sylvia, J. A. Janni, J. D. Klein and K. M. Spencer, *Anal. Chem.*, 2000, **72**, 5834–5840; (b) A. Hakonen, P. O. Andersson, M. S. Schmidt, T. Rindzevicius and M. Kall, *Anal. Chim. Acta*, 2015, **893**, 1–13.

21 (a) F. Qiu, Y.-H. Huang, Q. M. Ge, M. Liu, H. Cong and Z. Tao, *Spectrochim. Acta, Part A*, 2020, **226**, 117583; (b) V. Bharadwaj, J. E. Park, S. K. Sahoo and H.-J. Choi, *ChemistrySelect*, 2019, **4**, 10895–10901.

22 (a) A. Kumar, A. Kumar and D. S. Pandey, *Dalton Trans.*, 2016, **45**, 8475–8484; (b) N. Goel and N. Kumar, *Inorg. Chim. Acta*, 2017, **463**, 14–19.

23 (a) S. Senthilkumar, R. Goswami, N. L. Obasi and S. Neogi, *ACS Sustainable Chem. Eng.*, 2017, **5**, 11307–11315; (b) H.-R. Fu, L.-B. Yan, N.-T. Wu, L.-F. Ma and S.-Q. Zang, *J. Mater. Chem. A*, 2018, **6**, 9183–9191; (c) S. Xing, Q. Bing, H. Qi, J. Liu, T. Bai, G. Li, Z. Shi, S. Feng and R. Xu, *ACS Appl. Mater. Interfaces*, 2017, **9**, 23828–23835.

24 (a) Y. Wang, X. Chang, N. Jing and Y. Zhang, *Anal. Methods*, 2018, **10**, 2775–2784; (b) J. Li, L. Zhang, P. Li, Y. Zhang and C. Dong, *Sens. Actuators, B*, 2018, **258**, 580–588.

25 (a) K. Shanmugaraj and S. Abraham John, *New J. Chem.*, 2018, **42**, 7223–7229; (b) W. J. Zhang, S. G. Liu, L. Han, Y. Ling, L. L. Liao, S. Mo, H. Q. Luo and N. B. Li, *Anal. Methods*, 2018, **10**, 4251–4256.

26 (a) X.-D. Zhang, J.-A. Hua, J.-H. Guo, Y. Zhao and W.-Y. Sun, *J. Mater. Chem. C*, 2018, **6**, 12623–12630; (b) X. Yin, S. Meng and J. Xie, *Polyhedron*, 2018, **139**, 262–266; (c) L. Li, J. Cheng, Z. Liu, L. Song, Y. You, X. Zhou and W. Huang, *ACS Appl. Mater. Interfaces*, 2018, **10**, 44109–44115.

27 *CRC Handbook of Chemistry and Physics*, 95th edn, ed. W. M. Haynes, CRC Press LLC, Boca Raton, FL, 2014–2015, pp. 5–97.

28 (a) R. Sun, X. Huo, H. Lu, S. Feng, D. Wang and H. Liu, *Sens. Actuators, B*, 2018, **265**, 476–487; (b) A. Biswas, D. Giri, D. Das, A. De, S. K. Patra and R. Samanta, *J. Org. Chem.*, 2017, **82**, 10989–10996; (c) S. Kumar, N. Venkatramaiah and S. Patil, *J. Phys. Chem. C*, 2013, **117**, 7236–7245; (d) N. Wang, J.-C. Yang, L.-D. Chen, J. Li, Y. An, C.-W. Lu and Y.-Q. Tian, *New J. Chem.*, 2017, **41**, 2786–2792; (e) W. Xue, Y. Zhang, J. Duan, D. Liu, Y. Ma, N. Shi, S. Chen, L. Xie, Y. Qian and W. Huang, *J. Mater. Chem. C*, 2015, **3**, 8193–8199.

29 (a) N. Venkatramaiah, A. D. G. Firmino, F. A. Almeida Paz and J. P. C. Tome, *Chem. Commun.*, 2014, **50**, 9683–9686; (b) V. Bhalla, H. Arora, H. Singh and M. Kumar, *Dalton Trans.*, 2013, **42**, 969–974; (c) S. Shanmugaraju, H. Jadhav, R. Karthik and P. S. Mukherjee, *RSC Adv.*, 2013, **3**, 4940–4950; (d) H. Ma, F. Li, L. Yao, Y. Feng, Z. Zhang and M. Zhang, *Sens. Actuators, B*, 2018, **259**, 380–386; (e) E. Hussain, Y. Li, C. Cheng, H. Zhuo, S. A. Shahzad, S. Ali, M. Ismail, H. Qi and C. Yu, *Talanta*, 2020, **207**, 120316.

30 (a) N. Venkatramaiah, S. Kumar and S. Patil, *Chem. – Eur. J.*, 2012, **18**, 14745–14751; (b) S. Shanmugaraju, S. A. Joshi and P. S. Mukherjee, *J. Mater. Chem.*, 2011, **21**, 9130–9138; (c) S. S. Babu and S. K. Shanmugam, *J. Mater. Chem. C*, 2017, **5**, 4788–4796; (d) Y. Chandrasekaran, N. Venkatramaiah and S. Patil, *Chem. – Eur. J.*, 2016, **22**, 5288–5294.

31 (a) R. Hu, J. L. Maldonado, M. Rodriguez, C. Deng, C. K. W. Jim, J. W. Y. Lam, M. M. F. Yuen, G. Ramos-Ortiz and B. Z. Tang, *J. Mater. Chem.*, 2012, **22**, 232–240; (b) H. Li, H. Wu, E. Zhao, J. Li, J. Z. Sun, A. Qin and B. Z. Tang, *Macromolecules*, 2013, **46**, 3907–3914.

32 (a) C. Y. K. Chan, J. W. Y. Lam, C. Deng, X. Chen, K. S. Wong and B. Z. Tang, *Macromolecules*, 2015, **48**, 1038–1047; (b) J. Li, J. Liu, J. W. Y. Lama and B. Z. Tang, *RSC Adv.*, 2013, 3, 8193–8196.

33 V. Vij, V. Bhalla and M. Kumar, *ACS Appl. Mater. Interfaces*, 2013, **5**, 5373–5380.

34 M. K. Chahal and M. Sankar, *Anal. Methods*, 2015, **7**, 10272–10279.

35 A. Pandith, A. Kumar, J. Y. Lee and H. S. Kim, *Tetrahedron Lett.*, 2015, **56**, 7094–7099.

36 A. K. Bandela, S. Bandaru and C. P. Rao, *Chem. – Eur. J.*, 2015, **21**, 13364–13374.

37 V. Mahendran and S. Shanmugam, *RSC Adv.*, 2015, **5**, 92473–92479.

38 V. Bhalla, H. Arora and M. Kumar, *RSC Adv.*, 2015, **5**, 32637–32642.

39 P. Vishnoi, M. G. Walawalkar, S. Sen, A. Datta, G. N. Patwari and R. Murugavel, *Phys. Chem. Chem. Phys.*, 2014, **16**, 10651–10658.

40 P. Vishnoi, M. G. Walawalkar and R. Murugavel, *Cryst. Growth Des.*, 2014, **14**, 5668.

41 P. Vishnoi, S. Sen, G. N. Patwari and R. Murugavel, *New J. Chem.*, 2015, **39**, 886.

42 S. Nagendran, P. Vishnoi and R. Murugavel, *J. Fluoresc.*, 2017, **27**, 1299–1305.

43 K. Ponnuvel, G. Banuppriya and V. Padmini, *Sens. Actuators, B*, 2016, **234**, 34–45.

44 S. S. Babu and S. Shanmugam, *ChemistrySelect*, 2018, **3**, 4075–4081.

45 W. Fang, W. Zhao, P. Pei, R. Liu, Y. Zhanga, L. Konga and J. Yang, *J. Mater. Chem. C*, 2018, **6**, 9269–9276.

46 X. Lu, G. Zhanga, D. Li, X. Tian, W. Ma, S. Li, Q. Zhang, H. Zhou, J. Wu and Y. Tian, *Dyes Pigm.*, 2019, **170**, 107641.

47 A. Shylaja, S. R. Rubina, S. S. Roja and R. R. Kumar, *Dyes Pigm.*, 2020, **174**, 108062.

48 A. S. Tanwar, S. Hussain, A. H. Malik, M. A. Afro and P. K. Iyer, *ACS Sens.*, 2016, **1**, 1070–1077.

49 M. Sathiyaraj, K. Pavithra and V. Thiagarajan, *New J. Chem.*, 2020, **44**, 8402–8411.

50 P. Kumar, D. Arya, D. Nain, A. Singh, A. Ghosh and D. Amilan Jose, *Dyes Pigm.*, 2019, **166**, 443–450.

51 J. Gao, X. Chen, S. Chen, H. Meng, Y. Wang, C. Li and L. Feng, *Anal. Chem.*, 2019, **91**, 13675–13680.

52 Y. Erande, S. Chemate, A. More and N. Sekar, *RSC Adv.*, 2015, **5**, 89482–89487.

53 K. Maiti, A. K. Mahapatra, A. Gangopadhyay, R. Maji, S. Mondal, S. S. Ali, S. Das, R. Sarkar, P. Datta and D. Mandal, *ACS Omega*, 2017, **2**, 1583–1593.

54 B. Gogoi and N. S. Sarma, *ACS Appl. Mater. Interfaces*, 2015, **7**, 11195–11202.

55 S. Kaur, A. Gupta, V. Bhalla and M. Kumar, *J. Mater. Chem. C*, 2014, **2**, 7356–7363.

56 S. Kaur, V. Bhalla, V. Vij and M. Kumar, *J. Mater. Chem. C*, 2014, **2**, 3936–3941.

57 A. Sil, D. Giri and S. K. Patra, *J. Mater. Chem. C*, 2017, **5**, 11100–11110.

58 S. Maity, M. Shyamal, D. Das, A. Maity, S. Dey and A. Misra, *New J. Chem.*, 2018, **42**, 1879–1891.

59 V. Kachwal, P. Alam, H. R. Yadav, S. S. Pasha, A. R. Choudhury and I. R. Laskar, *New J. Chem.*, 2018, **42**, 1133–1140.

60 A. Kathiravan, A. Gowri, T. Khamrang, M. D. Kumar, N. Dhenadhayalan, K.-C. Lin, M. Velusamy and M. Jaccob, *Anal. Chem.*, 2019, **91**, 13244–13250.

61 Y. Ma, Y. Zhang, X. Liu, Q. Zhang, L. Kong, Y. Tian, G. Li, X. Zhang and J. Yang, *Dyes Pigm.*, 2019, **163**, 1–8.

62 H. Li, R. Jia and Y. Wang, *Spectrochim. Acta, Part A*, 2020, **228**, 117793.

63 J. Pan, F. Tang, A. Ding, L. Kong, L. Yang, X. Tao, Y. Tian and J. Yang, *RSC Adv.*, 2015, **5**, 191–195.

64 P. Ghosh and P. Banerjee, *Anal. Chim. Acta*, 2017, **965**, 111–122.

65 D. C. Santra, M. K. Bera, P. K. Sukul and S. Malik, *Chem. – Eur. J.*, 2016, **22**, 2012–2019.

66 J. B. Arockiam and S. Ayyanar, *Sens. Actuators, B*, 2017, **242**, 535–544.

67 Y. Peng, A.-J. Zhang, M. Dong and Y.-W. Wang, *Chem. Commun.*, 2011, **47**, 4505–4507.

68 M. Dong, Y.-W. Wang, A.-J. Zhang and Y. Peng, *Chem. – Asian J.*, 2013, **8**, 1321–1330.

69 Z.-H. Fu, Y.-W. Wang and Y. Peng, *Chem. Commun.*, 2017, **53**, 10524–10527.

70 G. Chakraborty and S. K. Mandal, *ACS Omega*, 2018, **3**, 3248–3256.

71 B. Pramanik, S. Das and D. Das, *Chem. – Asian J.*, 2020, **15**, 4291–4296.

72 X. Cao, N. Zhao, H. Lv, Q. Ding, A. Gao, Q. Jing and T. Yi, *Langmuir*, 2017, **33**, 7788–7798.

73 S. S. Harmalkar, A. V. Naik, M. K. Nilajakar and S. N. Dhuri, *ChemistrySelect*, 2020, **5**, 8447–8454.

74 P. Sakthivel, K. Sekar, S. Singaravadivel and G. Sivaraman, *ChemistrySelect*, 2019, **4**, 3817–3822.

75 H.-L. Ding, L.-D. Chen, N. Wang, K. Li, Y. An and C.-W. Lü, *Talanta*, 2019, **195**, 345–353.

76 Jigyasa and J. K. Rajput, *Sens. Actuators, B*, 2018, **259**, 990–1005.

77 R. Ahmed, A. Ali, M. Ahmad, A. Alsalme, R. A. Khan and F. Ali, *New J. Chem.*, 2020, **44**, 20092–20100.

78 Y.-C. Wu, S.-H. Luo, L. Cao, K. Jiang, L.-Y. Wang, J.-C. Xie and Z.-Y. Wang, *Anal. Chim. Acta*, 2017, **976**, 74–83.

79 J.-F. Xiong, J.-X. Li, G.-Z. Mo, J.-P. Huo, J.-Y. Liu, X.-Y. Chen and Z.-Y. Wang, *J. Org. Chem.*, 2014, **79**, 11619–11630.

80 S. Chaudhary, H. Sharma and M. D. Milton, *ChemistrySelect*, 2018, **3**, 4598–4608.

81 R. Sodkhomkhum, M. Masik, S. Watchasit, C. Suksai, J. Boonmak, S. Youngme, N. Wanichacheva and V. Ervithayasuporn, *Sens. Actuators, B*, 2017, **245**, 665–673.

82 S. Zhang, H. Zhu, J. Huang, L. Kong, Y. Tian and J. Yang, *ChemistrySelect*, 2019, **4**, 7380–7387.

83 B. K. Kundu, R. Pragti, S. M. Mobin and S. Mukhopadhyay, *New J. Chem.*, 2019, **43**, 11483–11492.

84 A. S. M. Islam, M. Sasmal, D. Maiti, A. Dutta, B. Show and M. Ali, *ACS Omega*, 2018, **3**, 10306–10316.

85 A. Panigrahi, B. P. Sahu, S. Mandani, D. Nayak, S. Giri and T. K. Sarma, *J. Photochem. Photobiol., A*, 2019, **374**, 194–205.

86 M. Shyamal, D. Das, P. K. Giri, S. Maity and A. Misra, *Mater. Today Chem.*, 2019, **14**, 100193.

87 (*a*) H. Ma, C. He, X. Li, O. Ablikim, S. Zhang and M. Zhang, *Sens. Actuators, B*, 2016, **230**, 746–752; (*b*) Y. Ma, L. Zhao, Y. Li, J. Liu, Y. Yang and T. Chu, *Tetrahedron*, 2018, **74**, 2684–2691.

88 Q. Lin, X.-W. Guan, Y.-Q. Fan, J. Wang, L. Liu, J. Liu, H. Yao, Y.-M. Zhang and T.-B. Wei, *New J. Chem.*, 2019, **43**, 2030–2036.

89 A. Kumar and P. S. Chae, *Sens. Actuators, B*, 2017, **240**, 1–9.

90 P. Lasitha and E. Prasad, *RSC Adv.*, 2015, **5**, 41420–41427.

91 S. Maity, M. Shyamal, P. Mazumdar, G. P. Sahoo, R. Maity, G. S. Morán and A. Misra, *J. Mol. Liq.*, 2016, **224**, 255–264.

92 E. Zhang, P. Ju, P. Guo, X. Hou, X. Hou, H. Lv, J. Wang and Y. Zhang, *RSC Adv.*, 2018, **8**, 31658–31665.

93 M. Ghosh, S. Ta, M. Banerjee, M. Mahiuddin and D. Das, *ChemistrySelect*, 2018, **3**, 6145–6151.

94 R. Chopra, V. Bhalla, M. Kumar and S. Kaur, *RSC Adv.*, 2015, **5**, 24336–24341.

95 Y. Ma, Y. Zhang, L. Kong and J. Yang, *CrystEngComm*, 2019, **21**, 94–101.

96 J. Du, J. Liu, Y. Ren, C. Wang, F. Bai and H. Hao, *Spectrochim. Acta, Part A*, 2019, **211**, 287–290.

97 N. Nagamani, S. Lakshmanan, D. Govindaraj, C. Ramamoorthy, N. Ramalakshmi and S. A. Antony, *Spectrochim. Acta, Part A*, 2019, **207**, 321–327.

98 S. Kumari, S. Joshi, T. C. Cordova-Sintjago, D. D. Pant and R. Sakhuja, *Sens. Actuators, B*, 2016, **229**, 599–608.

99 S. K. Patil, D. V. Awale, M. M. Vadiyar, S. A. Patil, S. C. Bhise, A. H. Gore, G. B. Kolekar, J. H. Kim and S. S. Kolekar, *ChemistrySelect*, 2017, **2**, 4124–4130.

100 A. Kumar, A. Pandith and H.-S. Kim, *Sens. Actuators, B*, 2016, **231**, 293–301.

101 Y. Xu, B. Li, W. Li, J. Zhao, S. Sun and Y. Pang, *Chem. Commun.*, 2013, **49**, 4764–4766.

102 L. Ding, Y. Bai, Y. Cao, G. Ren, G. J. Blanchard and Y. Fang, *Langmuir*, 2014, **30**, 7645–7653.

103 S. Hussain, A. H. Malik, M. A. Afroza and P. K. Iyer, *Chem. Commun.*, 2015, **51**, 7207–7210.

104 N. Yan, J. Song, F. Wang, L. Kan, J. Song, W. Wang, W. Ma, W. Zhang and G. He, *Chin. Chem. Lett.*, 2019, **30**, 1984–1988.

105 V. Lakshmidevi, C. V. Yelamaggad and A. Venkataraman, *ChemistrySelect*, 2018, **3**, 2655–2664.

106 P. S. Hariharan, J. Pitchaimani, V. Madhu and S. P. Anthony, *J. Fluoresc.*, 2016, **26**, 395–401.

107 B. Roy, A. K. Bar, B. Gole and P. S. Mukherjee, *J. Org. Chem.*, 2013, **78**, 1306–1310.

108 R. Kumar, S. Sandhu, P. Singh, G. Hundal, M. S. Hundal and S. Kumar, *Asian J. Org. Chem.*, 2014, **3**, 805–813.

109 S. Sandhu, R. Kumar, P. Singh, A. Mahajan, M. Kaur and S. Kumar, *ACS Appl. Mater. Interfaces*, 2015, **7**, 10491–10500.

110 N. Tripathi, S. Sandhu, P. Singh, A. Mahajan, M. Kaur and S. Kumar, *Sens. Actuators, B*, 2016, **231**, 79–87.

111 S. Sandhu, R. Kumar, P. Singh and S. Kumar, *J. Mater. Chem. C*, 2016, **4**, 3209–3216.

112 N. Tripathi, P. Singh and S. Kumar, *New J. Chem.*, 2017, **41**, 8739–8747.

113 S. Mukherjee, A. V. Desai, A. I. Inamdar, B. Manna and S. K. Ghosh, *Cryst. Growth Des.*, 2015, **15**, 3493–3497.

114 S. Dhiman, G. Kumar, V. Luxami, P. Singh and S. Kumar, *New J. Chem.*, 2020, **44**, 10870–10877.

115 S. Dhiman, M. Ahmad, G. Kumar, V. Luxami, P. Singh and S. Kumar, *J. Mater. Chem. C*, 2021, **9**, 1097–1106.

116 S. Sharma, G. Dubey, B. S. Sran, P. V. Bharatam and G. Hundal, *ACS Omega*, 2019, **4**, 18520–18529.

117 R. Purkait, A. Dey, S. Deya, P. P. Ray and C. Sinha, *New J. Chem.*, 2019, **43**, 14979–14990.

118 V. Bhalla, S. Kaur, V. Vij and M. Kumar, *Inorg. Chem.*, 2013, **52**, 4860–4865.

119 M. Kumar, S. I. Reja and V. Bhalla, *Org. Lett.*, 2012, **14**, 6084–6087.

120 S. Kasthuri, P. Gawas, S. Maji, N. Veeraiah and N. Venkatramaiah, *ACS Omega*, 2019, **4**, 6218–6228.

121 M. Hengchang, Z. Zhongwei, J. Yuanyuan, Z. Lajia, Q. Chunxuan, C. Haiying, Y. Zengming, Y. Zhiwang and Z. Lei, *RSC Adv.*, 2015, **5**, 87157–87167.

122 S. Madhu, A. K. Bandela and M. Ravikanth, *RSC Adv.*, 2014, **4**, 7120–7123.

123 X. Sun, X. Ma, C. V. Kumar and Y. Lei, *Anal. Methods*, 2014, **6**, 8464–8468.